The Effect of Hydrate Formation on Gas Relative Permeability in Porous Media

by

Najlla Ali

Submitted in partial fulfilment of the requirements
for the degree of Master of Applied Science

at

Dalhousie University
Halifax, Nova Scotia
April 2017

Dedicated to my family

Table of Contents

List of Tables

List of Figures

Abstract

Knowledge of permeability in hydrate bearing sediments has recently become indispensable for evaluating gas production and sequestration opportunities. Variation in gas permeability in Wallace sandstone samples exposed to hydrate formation was experimentally studied. The experiments were performed in a core flooding system. The relative permeability of CO_2 at residual water saturation was measured first at 20°C. Then the gas permeability measurements were repeated during hydrate formation at 3 and 4°C. Experimental results show that it was possible to form CO_2 hydrate in Wallace sandstone cores at injection pressure above 290 psi at temperatures of 3 and 4°C. All experimental data show that hydrate formation significantly reduces the permeability of porous media. Also, the results show that the amount of hydrate formation depends on the water content in the porous media. The experimental data show that permeability reduction was almost the same at 3 and 4°C at the same water content, which means that small temperature changes have relatively a small impact on the amount of hydrate formation. However, due to thermodynamic equilibrium, there is a sharp transition between conditions for hydrate formation and conditions that prevent hydrate formation.

List of Abbreviations and Symbols Used

A	cross sectional area of the core (m^2)
BPR	back pressure regulator
CFS	core flooding system
K_a	monophasic permeability (mD)
K_{eff}	effective permeability (mD)
K_r	relative permeability
M	molecular weight (kg $kmol^{-1}$)
NGH	natural gas hydrate
Q	volumetric flow rate (m^3 s^{-1})
Q_o	outlet flow rate of the core (m^3 s^{-1})
R	gas constant (Pa s $kmol^{-1}$ K^{-1})
L	length of the core (m)
m	mass flow rate (kg s^{-1})
M_{dry}	dry weight of the core (g)
M_{wet}	wet weight of the core (g)
P_1	upstream pressure (psi)
P_2	downstream pressure (psi)
P_c	capillary pressure
T	temperature (K or ºC)
V_p	pore volume (cm^3)
V_b	bulk volume (cm^3)
Z	compressibility factor
μ	viscosity (kg m^{-1} s^{-1})
ρ	density (g cm^{-3})
Φ	porosity
ΔP	pressure drop (psi)

Acknowledgments

I would like first to thank my supervisors, Dr. Michael Pegg and Dr. Jan Haelssig, for providing me such an interesting subject for my thesis. Thank you very much for all the guidance, patience and encouragement.

I would like also gratefully to thank Mr. Matt Kujath for his technical advice and support during the experimental stage.

I appreciate so much Mr. Ray Dube for being more than helpful. A lot of time was saved by helping me designing the cooling system for the experiment.

At the end, my deepest gratitude goes to my family and friends for their encouragement throughout my studies.

Chapter 1 Introduction

1.1 Introduction

Recently, there has been a great deal of interest in reservoir engineering to study the kinetics of gas hydrate formation within porous media and to understand how hydrate saturation affects the transport properties of the media. Many studies have considered the use of hydrate technology as a method of transportation and storage natural gas as well as carbon dioxide (CO_2) sequestration (Rajnauth *et al.*, 2010). In recent years, geological storage of carbon dioxide has become one of the most promising ways to reduce carbon dioxide emissions into the atmosphere. However, CO_2 hydrates can form during the process of storage and that could affect the characteristics of CO_2 injection and the pore structure properties of the porous media.

Due to increasing energy demand in the world, more and more researchers are also investigating methods to produce natural gas (NG) from hydrate deposits that occur naturally in the earth. Producing NG from natural gas hydrate (NGH) reservoirs can be considered as a potential source of new and clean energy. Conversely, NGH reservoirs can pose a potential hazard because gas hydrate dissociation that can contribute to the global warming effect. Therefore, the study of hydrate formation and dissociation conditions is necessary in order to explore NG production from NGH reservoirs.

Natural gas hydrates may also form during transportation of the gas in pipelines. In this case, the hydrate can form and plug the line if the gas was not properly dehydrated. Removing these plugs is expensive and time consuming. Therefore, understanding the hydrate formation kinetics and blockage formation is also important for gas transportation. Moreover, understanding hydrate formation kinetics in natural gas reservoir especially those located in low temperature environments is very important due to the danger of hydrate formation in the wells of gas reservoir. Natural gas development can be associated with temperature decrease up to the hydrate formation conditions. Hydrate formation in natural gas reservoirs can influence on the sediments properties such as permeability; and therefore this can affect the reliability of the gas supply. Thus,

there is a need to understand the hydrate formation process and its effect on the reservoir permeability, and how this affects techniques for gas production and transport.

In order to be able to measure permeability alteration due to gas hydrate formation it is important to mimic natural conditions of the reservoir in the laboratory. Core flooding experiments allow laboratory experiments to be performed at reservoir conditions. In this study, core flooding experiments were performed with CO_2 at various conditions to investigate the impact of hydrate formation on core permeability and operating conditions on the formation of hydrate.

1.2. Research Objectives

The primary objectives of the research are:

1. To study the formation conditions (pressure and temperature) of carbon dioxide hydrates in porous media.
2. To determine the relative permeability of carbon dioxide displacing water without hydrate formation and under hydrate conditions, and to investigate permeability alteration due to accumulation of hydrates.
3. To investigate the effect of temperature changes on the amount of CO_2 hydrate formation in sandstone.

The knowledge obtained from this work is expected to be valuable in the development and use of hydrate technology and natural gas production from natural gas reservoirs. To achieve the mentioned objectives, the laboratory experiments were performed in a core flooding system (CFS) at various conditions with CO_2 gas.

1.3. Dissertation Organization

The remainder of this thesis is organized into six chapters and two appendixes.

Chapter 2 contains an introduction and necessary scientific background about gas hydrate and it also presents a general literature review that explains the mechanism of gas hydrate formation. Chapter 3 provides an overview of the concept of relative permeability and how it can be measured for gases flowing through porous media in laboratory

experiments. Chapter 4 describes the details of the experimental design system (Core Flooding System) and the experimental procedures that were used to make various measurements. Chapter 5 contains the results of the relative permeability measurements made under non hydrate forming conditions, as well as an analysis and discussion of these results. Chapter 6 contains the results, analysis and discussion of the relative permeability measurements made under hydrate forming conditions. Finally, Chapter 7 presents the main conclusion of this research and gives an outlook on future work. The raw experimental data and other supporting materials is provided in the appendices.

1.4. References

Rajnauth, J. J., Barrufet, M., & Falcone, G. (2010, January). Potential industry applications using gas hydrate technology. In *Trinidad and Tobago Energy Resources Conference*. Society of Petroleum Engineers.

Chapter 2 Gas Hydrate Background

This chapter provides basic information related to the gas hydrates with specific focus on the thermodynamic behavior of methane and carbon dioxide hydrates. It also provides an overview of different methods that can be used to form and study hydrates in the laboratory. Additionally, the related work on the kinetics of gas hydrate formation in bulk and in porous media is presented in this chapter.

2.1. What is gas hydrate?

Gas hydrates are an ice-like crystalline compound (also called clathrates) in which a large amount of gas is trapped inside the cages formed by water under appropriate conditions of high pressure and low temperature (Phirani *et al*., 2009).

Many gaseous compounds (such as methane, ethane, carbon dioxide, hydrogen sulphide and other gases that have small molecules) can be trapped by water clathrates through strong hydrogen bonding to form gas hydrates. Methane hydrates are considered to be the most common in nature and are widespread in the permafrost regions where the conditions favour their formation.

The reactions of hydrate formation are not stoichiometric and depend on trapped gas size. The hydrate crystal lattice structure consists of water molecules that are connected together through hydrogen bonding to form cages and each cage of crystal can hold up to one gas guest molecule that is linked to the water lattice by weak van der Waals forces. The gas hydrates exist in several structures that are recognized by the sizes and the arrangement of the cages. Pentagonal dodecahedron is the basic building block of the common hydrate structure (Blackwell, 1998). Three hydrate crystal structures have been found in nature. The three structures are: structure I which accommodate both of methane and carbon dioxide, structure II which allows the inclusion of propane and isobutene with methane and ethane, and structure H which contains high molecular weight gases such as iso-pentane (Salam, 2013). The most significant difference between normal ice and hydrate structures is that hydrates do not form if there is no gas, while ice can form as pure compounds at its freezing point.

2.2. Methane Hydrates

Methane hydrates (also called methane ice) are a frozen compound that is formed as a result of the combination of water and methane under specific conditions of temperature and pressure. The gas and water molecules are not chemically bound in the methane hydrate; but the result of trapping gas inside crystalline substances appears like ice which represents a highly concentrated form of methane (Ruppel, 2011). The majority of gas hydrates that are found in nature were formed from methane gas, and it is considered such a large amount that it could contribute significantly to solve the future energy demand as a kind of clean and reliable energy source. The following equation shows the reaction between methane and water to form methane hydrates.

$$CH_4 + n\,H_2O \rightarrow CH_4.\,n\,H_2O \qquad (1.1)$$

Where n is hydration number.

Very specific conditions are required to form methane hydrates and for them to remain stable in the environment. High pressure, low temperature and a sufficient amount of water and gas are essential factors that control methane hydrate formation and its stability. Figure 2.1 shows the phase diagram of methane hydrate. The graph shows the ranges of pressure and temperature where the hydrate is stable. It is clear that hydrates form at temperature above the freezing point of water and that higher temperatures are possible at higher pressures. Since pressure increases and temperature typically decreases with increasing the depth below the surface of the earth or ocean, in the natural environment, gas hydrates are commonly found in the permafrost and deep ocean environment.

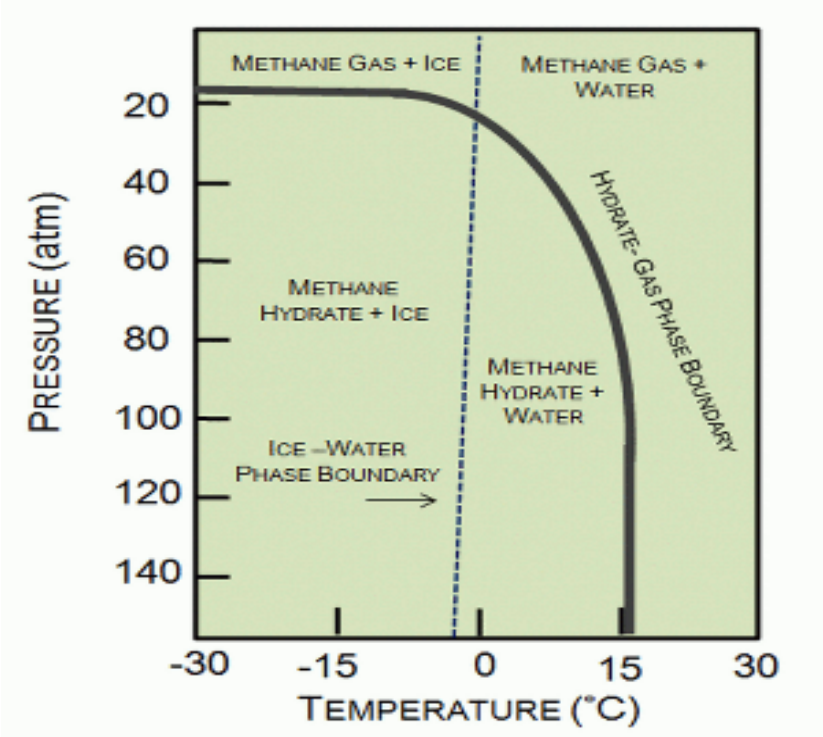

Fig. 2.1: Phase diagram for the methane-water system (Harrison, 2010).

Accumulation of natural gas hydrate (NGH) is found in places where the pressure above 40 atm and temperature is lower than 12°C. It is estimated that 99% of NGH is accumulated in oceanic sediments. Also, sufficient amounts of methane and water need to be present in order to form methane hydrates. Methane hydrates in nature can be formed through thermogenic or biogenic processes. The manufacture of thermogenic hydrocarbon gases occurs at depths exceeding 1000 m and they are produced under of high temperature and pressure from kerogens. The gas migrates through porous media until the conditions are suitable for hydrate formation. In contrast, biogenic hydrocarbon gases are produced as a result of bacterial activity. The process can take place under hydrate formation conditions, thus the gas does not migrate (Vadla, 2015).

2.3. Carbon Dioxide Hydrates

Carbon dioxide hydrates, $CO_2.nH_2O$ ($n \geq 5.75$) are nonstoichiometric compounds in which hydrogen bounded water molecules are arranged in an ice like framework forming cavities that are occupied by CO_2 gas molecules. CO_2 hydrates crystallizes to form a structure I in which the unit cell consists 46 H_2O molecules and up to 8 CO_2 molecules

(Circone *et al*., 2003). The thermodynamic conditions of CO_2 hydrates have been well studied experimentally and theoretically. Figure 2.2 shows the phase diagram for carbon dioxide hydrates formed in pure water.

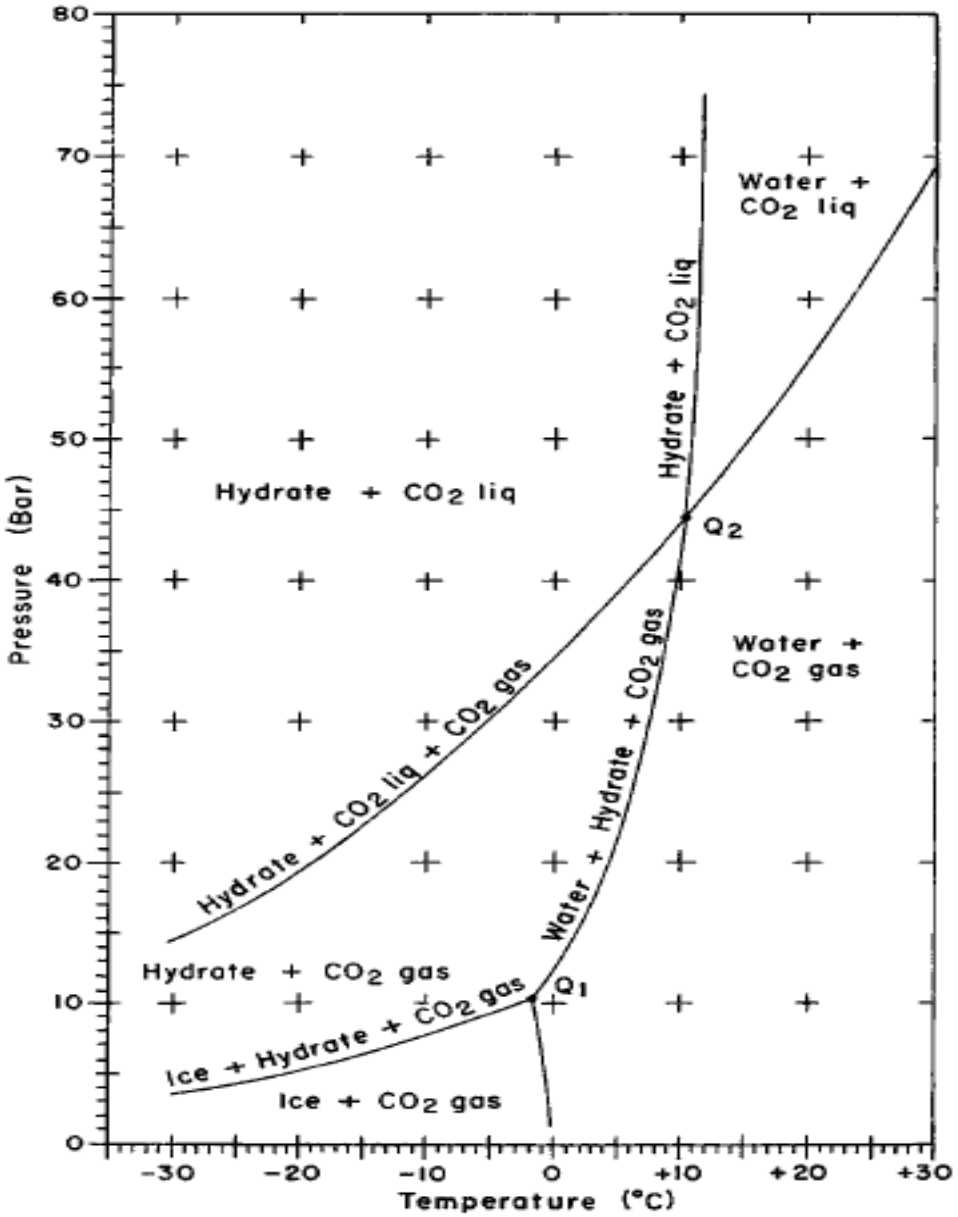

Fig. 2.2: Phase diagram for carbon dioxide hydrate in pure water (North *et al*., 1998).

Figure 2.2 shows that the system of water and carbon dioxide consists of the following possible phases: liquid water, ice water, hydrate, gaseous CO_2 and liquid CO_2.

It can be observed from the previous figures that the pressure and temperature stability region is different for CH_4 hydrates compared to CO_2 hydrates. At the same temperature, the formation pressure of CO_2 hydrates is significant lower than the formation pressure of CH_4 hydrates. The calculated formation pressure for pure CH_4 hydrate and pure CO_2 hydrate are 45 and 24.35 bar, at 4°C and 3.5wt% NaCl, respectively (Vadla, 2015). This estimation is based on bulk hydrates. The experiments in this thesis were performed with hydrates in porous media. Hydrate formation in porous media involves extra parameters including matrix structure and interconnectivity, pore networks and impurities, and therefore these parameters makes it is more difficult to predict the hydrate stability zone.

2.4. Hydrate Formation in Natural Gas Reservoirs

Hydrate formation can cause serious processing problems in the oil and gas industry. For example, hydrate formation during gas transportation can eventually plug pipelines, and thereby lead to costly loss and safety problems. However, chemical additives can be used to overcome such plugging conditions in pipelines (Salam *et al.*, 2013). Moreover, hydrates can form under some conditions in gas and oil reservoirs, which can impact the flow rate of the fluid into the wellbore area due to permeability decrease. Also, in CO_2 injection wells, hydrate formation can impact injection conditions.

Essentially, gas expansion due to pressure drop can contribute to temperature decrease, which is one of the essential factors controlling hydrate formation. In addition, hydrate formation in the bottom hole zone arises due to the fact that many fields have sufficiently high pressure. In fact, hydrate formation in this region can cause lowering of flow rates and sometimes complete plugging the path of the fluid into the well, which leads to reduce natural gas production.

2.5. Hydrate Formation Methods in the Laboratory

Different methods can be followed to form hydrates in controlled environments. In this section, various methods that can be used to form hydrates in the laboratory will be presented and examined (Kneafsey, 2012).

2.5.1. Excess gas method

In this method, saturated sand is placed in a sleeve or vessel. Hydrate forming gas is injected. Hydrate can be formed either by pressurizing the sample above the required pressure and then cooling the system, or pressurizing the already chilled sample.

By applying this method, it is expected that the sample will be uniformly saturated with hydrate due to the uniform distribution of the water in the sample. Also, this technique has been used for natural porous media, homogeneous and heterogeneous laboratory packed sand. Figure 2.3 shows two examples of hydrate formation.

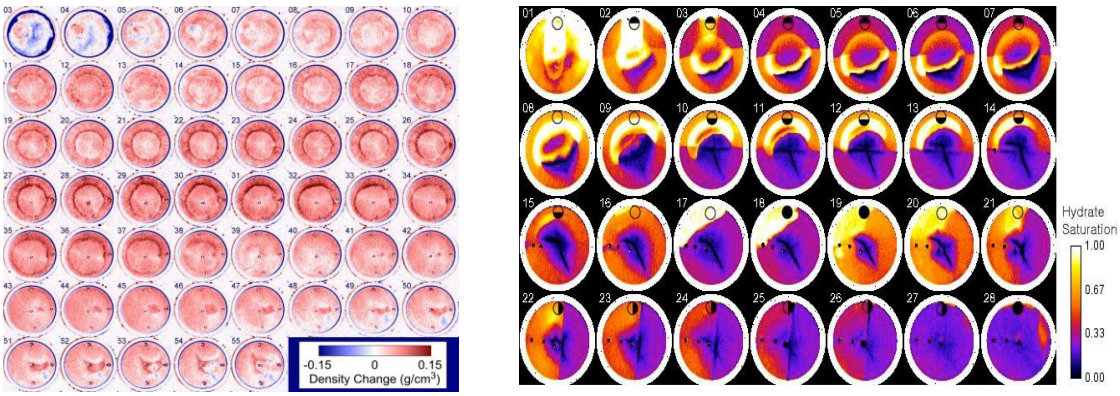

Fig. 2.3: Hydrate density change. Left: shows increasing hydrate formation density (red). Right: shows heterogeneous hydrate formation in heterogeneous sand packed (Kneafsey,2012).

2.5.2. Freeze/thaw/form hydrate

This method is similar to the excess gas method that is described above except that the sample is frozen and thawed by water prior to hydrate formation to provide nucleation sites throughout the sample. These sites will allow hydrate to start forming in many locations at the same time (see Figure 2.4).

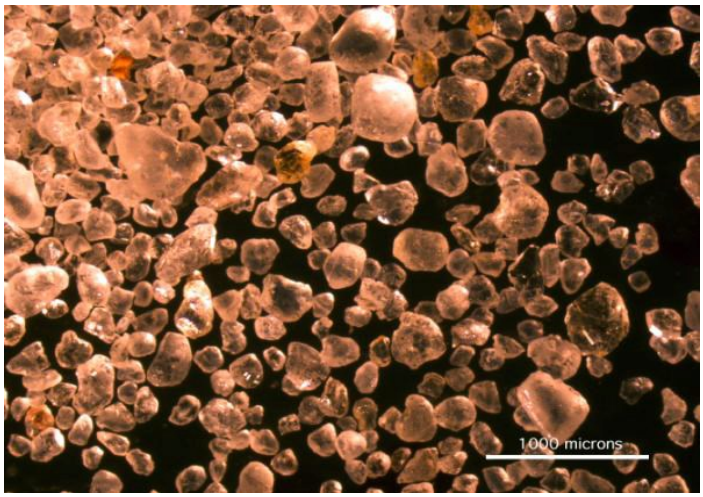

Fig. 2.4: Freeze/thaw/form hydrate method (Kneafsey, 2012).

2.5.3. Unsaturated- freeze/ pressurize/ thaw

In this method, confining pressure is applied on the moist sample packed in the sleeve and the sample is cooled until it is frozen. Then, the frozen sample is pressurized by introducing hydrate-forming gas. The temperature should be adjusted to allow melting ice to provide hydrate seeds for nucleation and the hydrate forms in the locations of melting ice in the presence of the gas at stability conditions of these locations.

2.5.4. Excess water method

In this method, dry sand is packed into a sleeve or pressure vessel and then a known quantity of the gas is added to the sample. After that, water is injected at the hydrate formation pressure and the sample is cooled. In this way, the distribution of gas and water is not uniform and this results in the formation of hydrate in locations where gas is trapped. For this reason, the hydrate saturation is expected to be heterogeneous.

2.5.5. Use of water containing salt

In this method, hydrate is formed by using the excess gas method but using brine instead of pure water. It is known that salts are hydrate inhibitors but the idea behind this method is that if the hydrates start forming in one location, then the concentration of salt in this location will stop or slow the formation of hydrate locally. This will allow to form

hydrate in other locations having dilute concentration of salt, resulting in a uniform hydrate distribution throughout the sample at the end.

2.6. Mechanism of Bulk Hydrate Formation

The kinetics of hydrate formation processes can be described based on crystallization theory. The crystallization can be separated into two stages, including nucleation and crystal growth. They are the most studied phenomena of gas hydrate formation.

The nucleation stage is the first step in the formation of a new thermodynamic phase or new structure. Typically, nucleation can be defined as a stochastic process that determines how long to wait before new phase or self-organized structures appear. In the hydrate formation process, the period that is required for crystal nuclei to form and achieve a critical size is called nucleation. Growth of these small nuclei into a network of larger hydrate crystals is called gas hydrate or crystal growth.

The time from first contact of gas and water to the first detection of hydrate phase called induction time and it has been used to measure nucleation period. The ability to predict the onset of nucleation in the gas industry is one of the most challenging aspects of flow assurance (Mork, 2002).

The kinetic process of hydrate formation is controlled by many factors. Recently, a lot of efforts have been made in understanding the dominating phenomena of hydrate formation but this subject has not been fully resolved yet. Based on the literature review, the driving force of the hydrate formation process is different among various studies. Vysniauskas and Bishnoi (1983) measured the rate of methane hydrate formation in a semi stirred batch reactor. They found that the gas hydrate formation kinetics were dominated by several factors including pressure, temperature, gas water contact area and subcooling. Kashchiev and Firoozabadi (2002) investigated the driving force of gas hydrate crystallization and they considered a three-phase system of hydrate forming gas, aqueous solution of gas and gas hydrate crystal (see Figure 2.5).

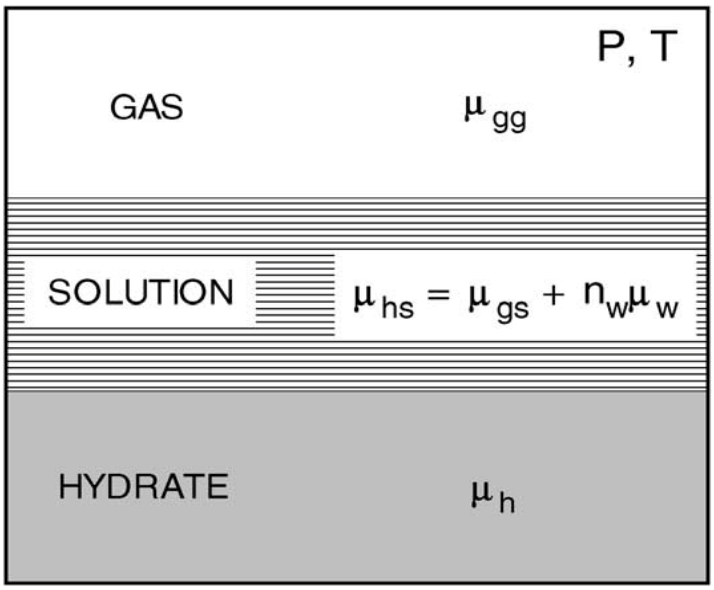

Fig. 2.5: Three phase system of gas hydrate process (Kashchiev & Firoozabadi, 2002).

They assumed that the driving force of hydrate formation is the difference in chemical potential ($\Delta\mu$) of hydrate building unit in the solution (μ_{hs}) and hydrate building unit in hydrate crystal (μ_h). Since the chemical potential depends on the concentration, so it can be said that the concentration of the gas in the solution determines the hydrate growth rate. Freer *et al*., (2011) investigated the growth rate of a methane hydrate film at the water-gas interface. Their results showed that the hydrate formation rate is a stronger function of heat transfer. Therefore, the difference between bulk temperature and equilibrium temperature is the driving force of hydrate formation. Furthermore, Myer (2011) used a bubble column to produce CO_2 gas hydrate at temperature around 4°C and they selected CO_2 as a model gas for safety purposes. Their results indicated that the heat removal controlled the hydrate formation rate rather than interphase mass transfer at high gas velocity and low temperature. While at low gas velocity, the hydrate formation rate was limited by mass transfer. Mork (2002) determined the rate of methane hydrate and natural gas hydrate formation by using a 9.5 L stirred tank reactor. In his experiments the rate of hydrate formation was measured at pressures between 70 and 90 bar and temperatures between 7 and 15°C. Their experimental results showed that the hydrate formation rate is strongly controlled by the rate of gas injection and pressure. Also, the result indicated that the rate of hydrate formation is not influenced by hydrate

concentration and gas composition. Mohebbi *et al.* (2015) conducted several experiments to study hydrate formation on mixtures of natural gas including methane, ethane and propane at different conditions. They assumed in their work that transportation of gas molecules from the gas phase to the aqueous phase is the controlling resistance. As the study was performed under isothermal conditions so, the heat transfer resistance was eliminated and the hydrate formation rate was determined by mass transfer. The mass transfer mechanism can be represented by six steps: (1) mass transfer from gas phase to gas water interface; (2) thermodynamic equilibrium at gas-liquid interface; (3) mass transfer from the gas-water interface; (4) gas molecules transfer in the bulk of aqueous phase; (5) mass transfer around the hydrate particles; and (6) hydrate formation reaction. Figure 2.6 illustrates these steps in terms of the concentration, Mohebbi *et al.* (2015) assumed that the third step is the limiting resistance among others. Figure 2.7 shows the process of hydrate formation with consideration of the controlling step.

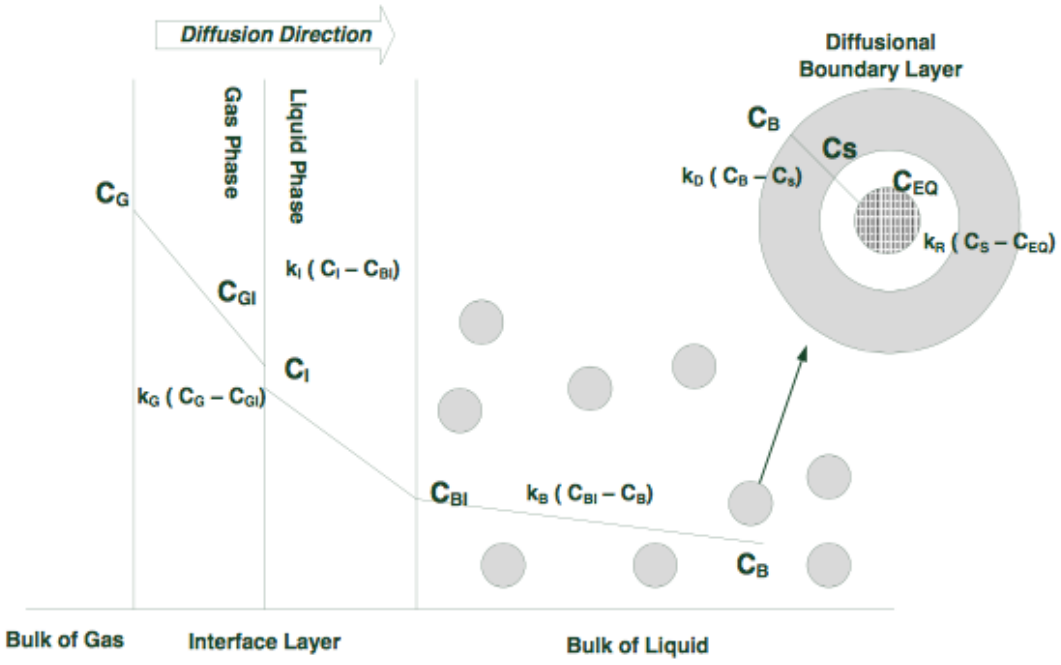

Fig. 2.6: Schematic diagram of mass transfer during hydrate growth; C shows the concentration (Mohebbi *et al.*, 2015).

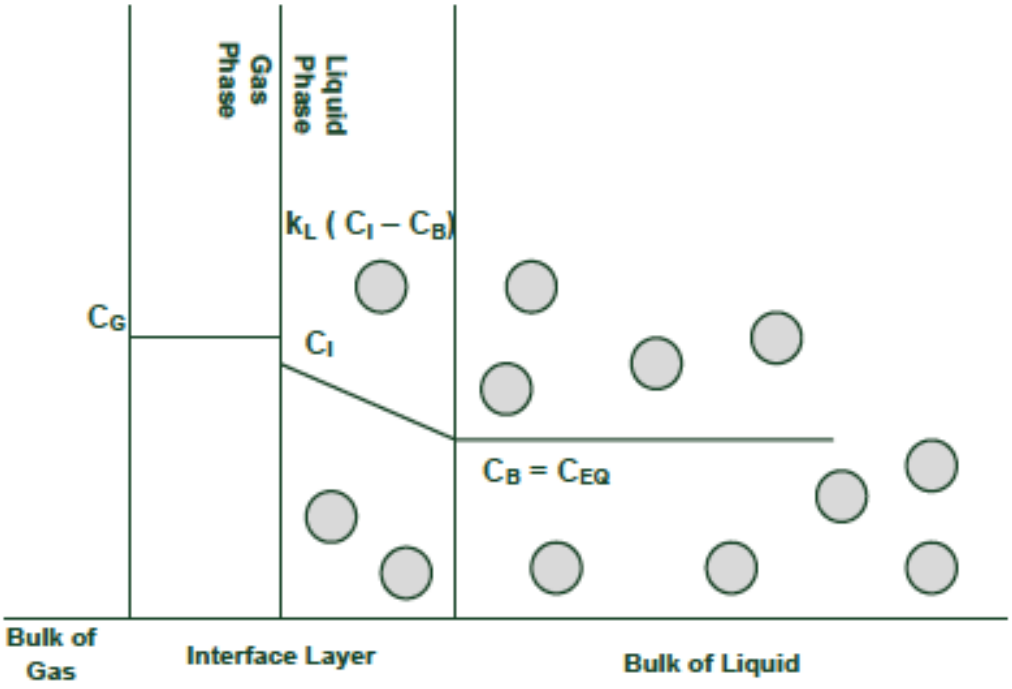

Fig. 2.7: Proposed concentration profile through hydrate formation process (Mohebbi *et al.,* 2015).

The studies mentioned above, and many other papers were mainly focused on hydrate formation in bulk phase (pure water), where the influence of heat transfer and mass transfer can be controlled. However, few studies have investigated the kinetics of hydrate formation in porous media, perhaps due to the difficulty of visualization and of estimation of the surface area of the hydrates inside porous media. Also, it is difficult to precisely control heat transfer and mass transfer. Conversely, in the bulk phase system, increasing the stirring speed inside a batch reactor can eliminate the effect of mass transfer and heat transfer (Li *et al.*, 2014).

2.7. Review of Hydrate Formation in Porous Media

Compared with bulk conditions, the phase behaviour of gas hydrate growth in porous media is much less understood. Research on kinetics of hydrate growth in porous media started only recently and it is still under development. Review of previous gas hydrate studies indicates that the formation rate of gas hydrates in porous media is controlled by many factors including temperature, pressure, availability of the gas and water, and the

presence of porous media. Many experiments were carried out to investigate the effect of different types of porous media and their properties on the rate of hydrate formation and equilibrium conditions. Mingjun *et al.* (2010) studied experimentally the hydrate formation conditions in porous media with different pore sizes and gas compositions to provide important data for understanding thermodynamic conditions of gas hydrate. The results indicate that decreasing pore size increases the equilibrium pressure when temperature and salinity are constant. Also, Bondarev and Savvin (2002) determined the effect of moisture content in porous media on the temperature of hydrate dissociation at a given pressure. It was found in Makgogn's study (1974), as cited in Bondarev and Savvin (2002), that the temperature of hydrate formation in the rock sand was 2.5 K lower than in the absence of porous media. Eaton *et al.* (2005) designed a new experimental apparatus, named FISH (Flexible Integrated Study of Hydrate) to study the kinetics of formation and dissociation of methane hydrates in the artificial and natural sediments.

In addition, Nam *et al.* (2008) studied the kinetics of methane hydrate formation and decomposition in the presence of silica sand particles at three different temperatures. In that paper, the conversion of water to hydrate during the experiment was estimated by using gas uptake data. The experimental results showed that the conversion of water to hydrate was 11, 78.5 and 79.8% mole for the experiments conducted at temperature 7, 4 and 1ºC, respectively. The results indicate that the extent of hydrate formation achieves the same level at 1ºC and 4ºC. Waite and Spangenberg (2013), concluded that the rates of the hydrate formation in the laboratory and natural environment are controlled by the concentration of the dissolved methane gas in the water. They indicated in their conclusion that the amount of dissolving methane gas in the circulating water is more important than temperature, pressure and the condition of the fluid flow.

However, there is only limited information on the kinetic of gas hydrate formation, especially for gas flow through saturated porous media. This work aims to investigate the CO_2 hydrate conditions during the displacement process in porous media and the influence of hydrate formation on porous media permeability. Carbon dioxide hydrate was chosen as a model due to safety concerns for methane and lower hydrate forming pressure. This kind of study is expected to be helpful in many other applications.

2.8. References

Blackwell, V. (1998). Formation processes of clathrate hydrates of carbon dioxide and methane. California Institute of Technology.

Bondarev, E., Rozhin, I., & Argunova, K. (2008). Prediction of Hydrate Plugs in Gas Wells in Permafrost. In *6th International Conference on Gas Hydrates*.

Circone, S., Stern, L. A., Kirby, S. H., Durham, W. B., Chakoumakos, B. C., Rawn, C. J. (2003). CO_2 hydrate: synthesis, composition, structure, dissociation behavior, and a comparison to structure I CH_4 hydrate. *The Journal of Physical Chemistry B*, *107*(23), 5529-5539.

Eaton, M., Mahajan, D., & Flood, R. (2007). A novel high-pressure apparatus to study hydrate–sediment interactions. *Journal of Petroleum Science and Engineering*, *56*(1), 101-107.

Freer, E. M., Selim, M. S., & Sloan, E. D. (2001). Methane hydrate film growth kinetics. *Fluid Phase Equilibria*, *185*(1), 65-75.

Harrison, S. E. (2010). Natural Gas Hydrates. *Coursework Physics 240, Stanford University*.

Kneafsey, T. J. (2012). Examination of Hydrate Formation Methods: Trying to Create Representative Samples.

Kashchiev, D., & Firoozabadi, A. (2002). Driving force for crystallization of gas hydrates. *Journal of crystal growth*, *241*(1), 220-230.

Li, B., Li, X. S., & Li, G. (2014). Kinetic studies of methane hydrate formation in porous media based on experiments in a pilot-scale hydrate simulator and a new model. *Chemical Engineering Science*, *105*, 220-230.

Mork, M. (2002). Formation rate of natural gas hydrate-reactor experiments and models.

Mohebbi, V., & Mosayebi Behbahani, R. (2015). Measurement of Mass Transfer Coefficients of Natural Gas Mixture during Gas Hydrate Formation. *Iranian Journal of Oil & Gas Science and Technology*, *4*(1), 66-80.

Myre, D. (2011). Synthesis of carbon dioxide hydrates in slurry bubble column.

Mingjun, Y., Yongchen, S., Yu, L., Yongjun, Chen., & Qingping, L. I. (2010). Influence of pore size, salinity and gas composition upon the hydrate formation conditions. *Chinese Journal of Chemical Engineering*, *18*(2), 292-296.

Nam, S. C., Linga, P., Haligva, C., Ripmeester, J. A., & Englezos, P. (2008). Kinetics of hydrate formation and decomposition of methane in silica sand.

North, W. J., Blackwell, V. R., & Morgan, J. J. (1998). Studies of CO_2 hydrate formation and dissolution. *Environmental science & technology*, *32*(5), 676-681.

Phirani, J., Pitchumani, R., & Mohanty, K. K. (2009, January). History matching of hydrate formation and dissociation experiments in porous media. In *SPE Reservoir Simulation Symposium*. Society of Petroleum Engineers.

Ruppel, C. (2011). Methane hydrates and the future of natural gas. *MITEI Natural gas Report, Supplementary Paper on Methane Hydrates*, *4*, 25.

Salam, K. K., Arinkoola, A. O., Araromi, D. O., & Ayansola, Y. E. (2013). Prediction of Hydrate Formation Conditions in Gas Pipelines. *International Journal of Engineering*, *2*(8), 327-331.

Vysniauskas, A., Bishnoi, R. (1983). A kinetic-study of methane hydrates formation. Chem. Eng.Sci.38(7),1061–1072.

Vadla, E. R. (2015). An Experimental Study of Methane Hydrate Growth and Dissociation in Porous Media. Bergen University

Waite, W. F., & Spangenberg, E. (2013). Gas hydrate formation rates from dissolved-phase methane in porous laboratory specimens. *Geophysical Research Letters*, *40*(16), 4310-4315

Chapter 3 Theory

This chapter aims to provide information about relative permeability and why it is important to be considered in gas and oil production. Also, the foundations of fluid flowing (liquid/gas) through porous media will be explained using Darcy's law. In addition, previous work on relative permeability will be presented at the end of this chapter.

3.1 Darcy's Law and Permeability

Basically, Darcy's law is the fundamental equation that describes the flow of fluid in porous media.

$$Q = -\frac{KA}{\mu}\frac{dP}{dL} \tag{3.1}$$

where Q is the volumetric flow rate (m^3/s), K is the permeability (m^2), A is the cross-sectional area (m^2), μ is the dynamic viscosity (Pa s), dP is the differential pressure (Pa), and dL is the length (m).

The minus sign (-) in front of the pressure gradient term indicates that fluid flows down the pressure gradient in the direction of flow. Assuming homogeneous porous media and constant liquid flow rate Q (as shown in Figure 3.1), the integration from position 1 to 2 is written as follows:

$$\frac{dP}{dX} = \frac{P_2 - P_1}{X_2 - X_1} = -\frac{P_1 - P_2}{X_2 - X_1}$$

where $P_1 > P_2$ so the sign (-) is needed to balance the equation.

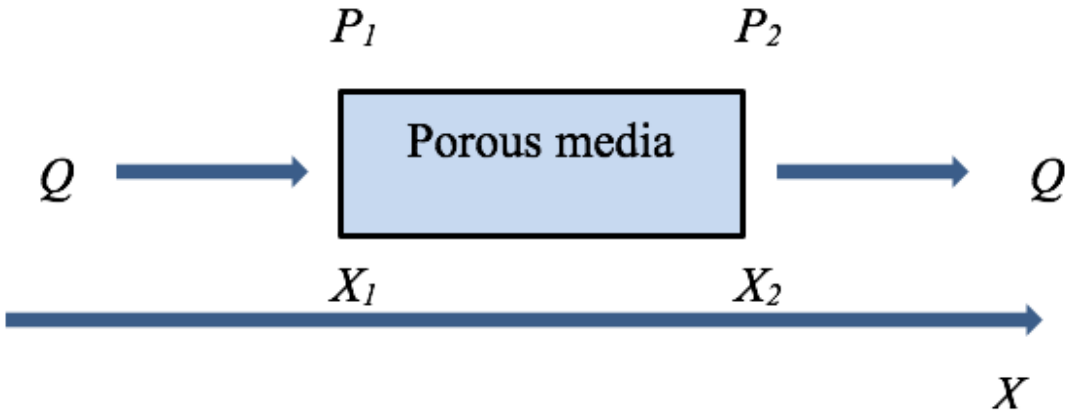

Fig. 3.1: Horizontal flow in core sample.

Permeability, *K,* is related to transport capability of porous media. It is one of the critical properties of reservoir rocks, and depends on the size of interconnected pores, geometry, capillaries as well as fractures. The permeability provides a measure of a fluid's ability to move through porous media and it is an important property of porous materials that governs the flow of fluids through hydrocarbon reservoirs and aquifers. Also, the measurement of *K* allows reservoir engineers to determine the flow capacity of gas or oil in the reservoirs.

The common unit of permeability is the Darcy (10^{-12} m^2). It has units of area because that is related to the area of the pore space in the cross section. The unit Darcy is named for the French engineer Henry Darcy, who performed many experiments involving the flow of water through porous media, and his experiments led to formulation Darcy's law that describes the flow of fluids through porous media at steady state. Practically, milli-Darcy (mD) is the common unit used in oilfield applications.

The permeability of porous media saturated with one phase is called absolute permeability, K_a, and it can be measured directly in the laboratory using Darcy's law, (Equation 3.1). For incompressible fluids, experiments are normally performed under the following conditions:

1. Horizontal flow.
2. 100% fluid saturation in the porous media.

3. Constant cross sectional area.
4. Laminar flow.
5. No reactions between the fluid and porous media.

Having all of the above conditions, the permeability can be calculated from the experimental data by using the following formula:

$$Q = -\frac{KA}{\mu L}\,\Delta P \tag{3.2}$$

where the flow rate, Q, and the pressure difference, ΔP, are the measured data. Permeability is estimated by plotting the measured data as shown in Figure 3.2.

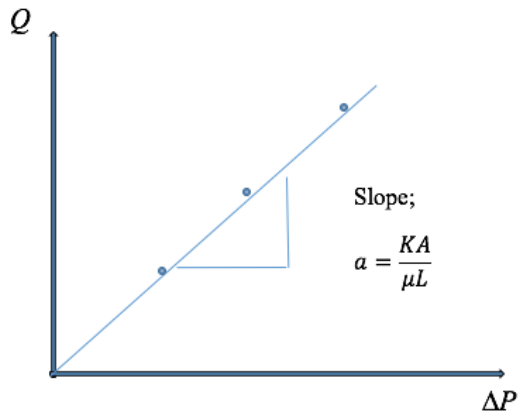

Fig. 3.2: Experimental determination of liquid permeability

In most reservoirs, multiphase flow is common. Therefore, it is important to consider effective and relative permeability to evaluate multi-phase systems. Effective permeability is defined as a measure of the conductivity of porous media for one fluid in the presence of other fluids in the media. While relative permeability, K_{ri}, is defined as a ratio of the effective permeability of the fluid to a base permeability. So, K_r, is a dimensionless number and it normally ranges between 0 to 1. Basically, the concept of relative permeability accounts for the reduction in effective permeability of each phase relative to absolute permeability due to presence of other phases.

Additionally, it is important to mention the concept of wettability, which is the preference of the solid phase to be in contact with one fluid phase rather than others in multiphase flow. So, the wettability can affect the local distribution of the phases that may have impact on the relative abilities of fluids to flow through the media.

Darcy's law can be written for each phase, *i*, in a multiphase system as:

$$Q_i = \frac{K_a K_{ri}\, A}{\mu_i} \frac{dP}{dL} \tag{3.3}$$

Where K_{ri}, is relative permeability for each phase and K_a, is absolute permeability.

3.2. Wettability

A simple way to model flow through porous media is to assume that the small pores in reservoir rock are similar to capillary tubes and they commonly contain two immiscible fluids in contact to each other. Capillary pressure is a significant factor controlling fluid distribution in reservoir rocks. It can be defined as the difference in pressure between two immiscible fluid phases resulting from the interfacial tension between two phases that should be overcome to initiate flow. The capillary pressure equation can be written as follows:

$$P_c = P_{non-wetting\ phase} - P_{wetting\ phase} \tag{3.4}$$

The wetting phase is the phase that preferentially covers more of the solid surface rather than the other phase. In an oil-water system, typically water is wetting phase and oil is non-wetting phase.

Gas cannot penetrate a porous media that is initially saturated with water until the capillary pressure exceeds the threshold pressure, which depends on the characteristics of the pores and the wettability of the media. As capillary pressure increases above this value, the saturation of the water starts to decrease. There is a general belief that the gas cannot flow until its saturation is above a critical value (5 to 15% of the total pore volume).

Capillary pressure controls fluid displacement in a reservoir. For the non-wetting phase invading wetting phase pores, the pressure in the non-wetting phase must be elevated relative to the wetting phase. Capillary pressure will change as the fluids or rocks change because these changes cause wettability and surface tension alteration. Under capillary effects, usually the non-wetting phase occupies the largest pathway (most permeable) while wetting phase imbibes into smallest and less permeable pathway. Figure 3.3 shows the fluid distribution at the pore scale for water invading as wetting phase and as non-wetting phase.

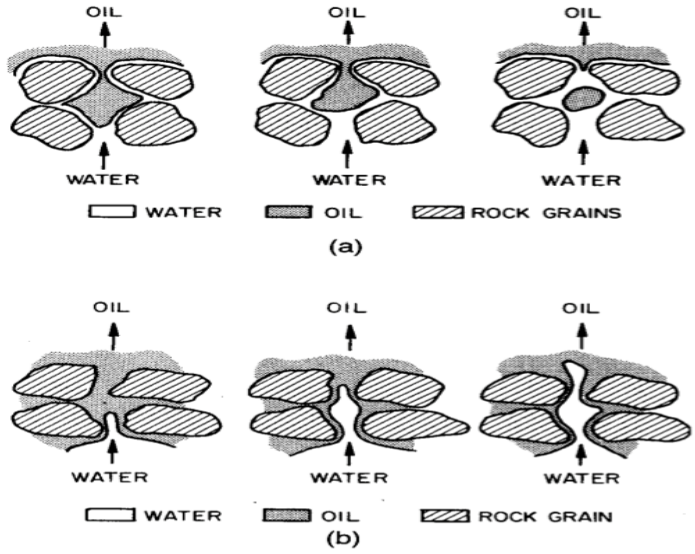

Fig. 3.3: Fluid distribution at pore scale for water (a) as wetting phase and (b) as non-wetting fluid (Levine, 2011).

At high saturation of invading phase, the fluid that has been invaded (wetting phase) becomes disconnected and stops to flow. The remaining undisplaced fluid at the endpoint saturation of invading phase blocks fluid pathways and this controls the end point relative permeability for the invading fluid. This means that an invading wetting phase is never able to fully displace a non-wetting phase from the largest and most permeable pores. Figure 3.4 presents the relative permeability curves for water invading rocks saturated with oil. To determine water-oil relative permeability, effective permeability should be measured over a range of fluid saturation. This figure illustrates that when water invades as the wetting phase, it is imbibed into the smallest pores and never accesses to the

largest pathways, which results in a lower endpoint relative permeability. Conversely, when water invades as the non-wetting phase, it can access the largest pathways, resulting in a high endpoint relative permeability. This indicates that measuring relative permeability provides a qualitative measure of wettability.

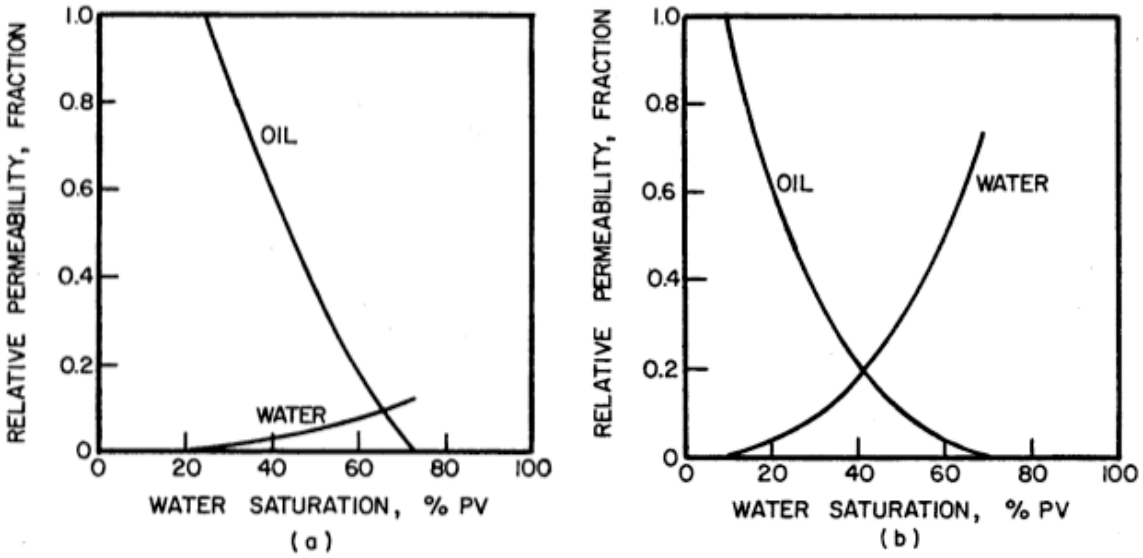

Fig. 3.4: Relative permeability curves for water invading oil (a) as wetting phase and (b) non-wetting fluid (Levine, 2011).

3.3. Steady and Unsteady State Water Flood Procedure

Laboratory measurements of relative permeability are made by displacing one phase with another (unsteady state test see Figure 3.5) or simultaneous flow of two phases (steady state test see Figure 3.6). As can be seen, in the unsteady state test, there is only one phase injected into the core and the saturation equilibrium is not achieved during the test. The outlet flow rate and the fluid composition is measured and used in estimating relative permeability. Figure 3.5. (b) shows an example of the relative permeability curve from an unsteady state experiment. At the beginning of the experiment, the core is saturated with 80% oil and 20% water that represents irreducible water saturation. Point A represents the relative permeability of oil at this condition and it is equal to unity. Point B represents the initial water permeability and it is equal to zero because irreducible water is immobile. Water is then injected at one end and the volumes of displacing fluid (water and oil) are measured at the other end of the core. As a result of this process, the

permeability of oil reduces to zero along the curve ACD, and the permeability of water increases along curve BCE.

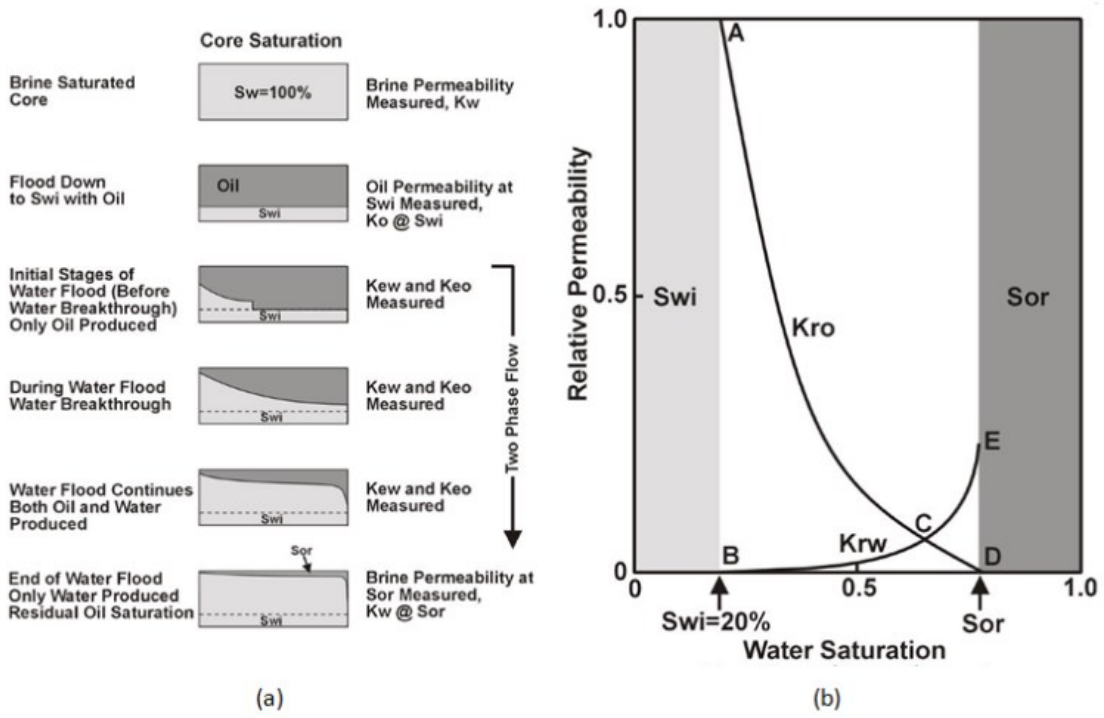

Fig. 3.5: (a) Unsteady state water flood procedure, (b) Typical relative permeability curve (Kantzas *et al.*, 2017).

Unsteady state is popular because it does not take much time and money to operate. However, the values obtained from these tests are less reliable because the system is not at steady state when the measurements are taken. Also, it is important to emphasize that Darcy's law is not applicable. The Buckley-Leverett equation for linear displacement is the basis for all calculations (Kantzas *et al.*, 2017).

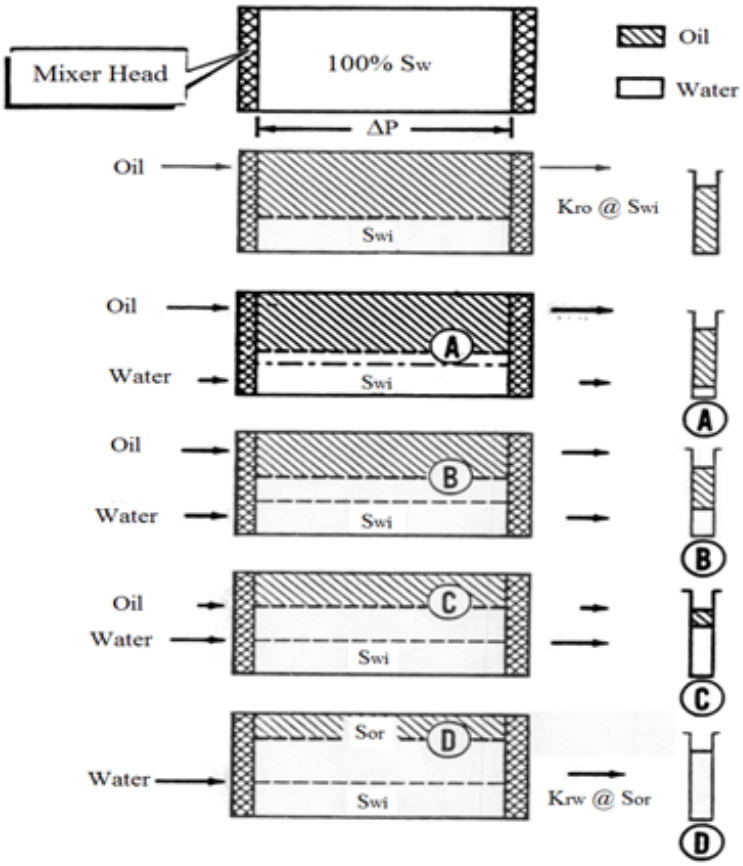

Fig. 3.6: Steady state water flood procedure (Kantzas *et al.*, 2017).

Conversely, the steady state test for measuring relative permeability is considered to be the most reliable source of relative permeability data. It is possible to apply Darcy's law to estimate the effective permeability for each phase at given saturation. Two phases are injected simultaneously into a test core at a constant rate and pressure. The system is assumed to be at steady state once pressure drop remains relatively constant. At this point the outlet flow rate of each phase and the pressure drop are measured. Darcy's law is used to calculate effective permeability of the fluid at that saturation. The inlet flow rate ratio is then changed and the process is repeated. In this way, the relative permeability curve can be obtained for each phase. The main problem associated with steady state experiments, is that the process can take a long time to stabilize to the steady state condition at a certain saturation level. However, it is definitely the most accurate technique for calculation of core permeability (Kantzas *et al.*, 2017).

3.4. Measuring CO_2 Endpoint Relative Permeability

Measuring drainage endpoint relative permeability requires achieving residual water saturation as well as avoiding capillary pressure effects by choosing a high Darcy flow rate through the core. To meet these requirements, the CO_2 pressure should be sufficiently elevated relative to the capillary pressure to invade the smallest pores. In addition, the pressure drop should not be so great that it completely overcomes the capillary pressure and displaces all of water in the core samples.

3.4.1. Ramakrishnan and Cappiello Method

The Ramakrishnan and Cappiello method is a steady state method developed in Ramakrishnan and Cappiello (1991) (Levine, 2011). This method is used to measure relative permeability with consideration of capillary end effects rather than avoid them. Capillary end effects result from discontinuities that exist at both ends of the core in core flooding experiments. It is known that capillarity causes pressure difference between the non-wetting and wetting phases, but this effect does not exist at the outlet of the core and therefore the two fluids will have the same pressure. So, the saturation of the wetting phase is higher at the end of the core than in the rest of the core. This method based on achieving uniform saturation throughout the core.

A constant non-wetting phase flow rate (CO_2) is injected at the front of the core that is saturated with wetting phase (water). The non-wetting phase will displace the wetting phase until reaching steady state. At steady state, the wetting phase does not flow for a given imposed flow rate or pressure ($Q_w = 0$) and all of the flow in the core will be due to the non-wetting phase, $Q = Q_{nw}$. The absence of flowing wetting phase means that wetting phase pressure is uniform throughout the core, $P_w = P - P_o = 0$. As a result, at steady state capillary equilibrium holds throughout the core and the pressure of the non-wetting phase must be matched with capillary pressure and Darcy's law can be applied for non-wetting phase. The relative permeability value for the invading phase is limited by an immobile residual amount of displaced fluid.

3.4.2 Modification of Darcy's law to Measure Gas Permeability

It is important to emphasize that Darcy's law was developed for flow of incompressible fluids through porous media. Since gas is a highly compressible substance, Darcy's law may not be applied directly for compressible gases. To solve this issue, it is important to think about mass flow rate because mass flow rate is constant and it is not proportional to pressure gradient for steady state flow.

A mathematical description of gas flow rate in porous media can be obtained by combining the following three principles:

1. Law of mass conservation (continuity equation)
2. Equation of state
3. Darcy's law

Darcy's law in differential form can be written as,

$$Q = -\frac{KA}{\mu}\frac{dP}{dL} \tag{3.5}$$

Considering mass flow of a gas, $Q\rho$, Darcy's law can be written as,

$$Q\rho = -\frac{KA\rho}{\mu}\frac{dP}{dL} \tag{3.6}$$

where ρ is the density of the gas at a certain pressure. Using ideal gas law ($Pv = nRT$), ($\rho = (\frac{\rho_0}{P_0}) * P$). Therefore, Darcy's law can be written in terms of mass flow rate by substituting $m = Q\ \rho$.

$$m = Q\rho = Q_o\rho_o = -\frac{KA\rho_0 P}{P_0\mu}\frac{dP}{dL} \tag{3.7}$$

The subscript (o) refers to a certain pressure value.

From the ideal gas of equation of state:

$$\rho = \frac{P_o M}{ZRT}$$

where *M*, is molecular weight (kg/kmol), and *Z*, is compressibility factor. Finally,

$$m\int_0^L dL = -\frac{KA}{RT}\int_{P_2}^{P_1}\frac{PdP}{\mu Z(P)} \tag{3.8}$$

where P_1 is inlet pressure and P_2 is the outlet pressure.

Note that viscosity and compressibility factor are functions of pressure. Therefore, to solve Equation 3.8, two approximations can be made. In the lower pressure region, μZ is approximately constant and can be calculated at average pressure of $\frac{P1+P2}{2}$ (Engler, 2010). In this case equation 3.8 can be written as the following;

$$mL = \frac{KAM}{2RT\mu Z}\,(P_1^2 - P_2^2) \tag{3.9}$$

The permeability of gas at steady state flow can be estimated from the slope of a plot of $m\ vs.\ (P_1^2 - P_2^2)$.

In multi-phase systems, *K* is the effective permeability. The equation can be written in terms of relative permeability as:

$$mL = \frac{K_a K_r AM}{2RT\mu Z}\,(P_1^2 - P_2^2) \tag{3.10}$$

However, for more accuracy, Equation 3.8 can be solved with consideration of the variation of (μZ) with pressure and temperature. The permeability values can be estimated from the slope of a plot of $\int \frac{\boldsymbol{PdP}}{\boldsymbol{\mu Z(P)}}$ and mass flow rate, *m*.

Appendix B contains three figures that show the variation of viscosity and compressibility factor with pressure at 3, 4 and 20ºC. The data was generated by using Honeywell UniSim Design R440. The viscosity and compressibility were estimated by

using the Ely and Hanley model and Peng-Robinson equation of state, respectively. The integral was evaluated numerically by using successive application of trapezoid rule with small enough step size to ensure accuracy to at least six significant figures.

So, Equation 3.8 can be written at different temperatures as follows:

$$mL = -\frac{KA}{RT}\int_{P_2}^{P_1} \frac{PdP}{-3.3452\mathrm{E}-12\mathrm{P}^2 - 3.4354\mathrm{E}-9\mathrm{P} + 1.3371\mathrm{E}-05} \tag{3.11}$$

$$mL = -\frac{KA}{RT}\int_{P_2}^{P_1} \frac{PdP}{-3.3035E-12P^2 - 3.3806E-9P + 1.3422E-05} \tag{3.12}$$

$$mL = -\frac{KA}{RT}\int_{P_2}^{P_1} \frac{PdP}{-2.4460E-12P^2 - 2.6590E-9P + 1.4252E-05} \tag{3.13}$$

Equations (3.11), (3.12) and (3.13) were developed at temperatures 3, 4 and 20ºC respectively.

3.5. Brine CO_2 Relative Permeability and the Influence of Hydrate on Gas Permeability

Generally, relative permeability measurements provide strong indication of the formation of gas hydrate in core samples. Many experiments in this study were performed to measure endpoint relative permeability of CO_2 displacing water rather than measuring relative permeability over the entire range of water saturation. This technique is based on achieving residual water saturation (irreducible water saturation) in the core. Then by applying Darcy's law, relative permeability can be estimated. Leaven (2011) conducted a series experiments in a core flooding system at different pressure conditions to measure endpoint relative permeability of CO_2 displacing water for synthetic and natural rock cores at ranges of pressures, temperature and salinities. He found that the endpoint relative permeability clustered between 0.35 to 0.4. Chuvilin *et al.* (2014) studied the influence of ice and hydrate formation on the gas permeability of sand and loamy sand

sediments. The results of his research showed that the gas permeability of sand and loamy sand sediments is decreased from 0.4 mD to 0.07 mD with water contents of 14-18% and 70% of pore water transformed into hydrate. Also, Johnson *et al.* (2011), modified an experimental setup to investigate the permeability characteristics of five unconsolidated cores from the Mount Elberta stratigraphic test well. They observed that hydrate saturations around 1.5 to 36% can significantly reduce the permeability of porous media. Rubble and Nimblett (2003) investigated the evolution of gas hydrate zones in porous media and their effect on the permeability numerically. Jaiswal *et al.* (2004) performed an experiment to allow gas hydrate to form in porous media for a relatively long time and relative permeability was measured at different hydrate saturations. Chuvilin & Grebenkin (2015) studied the variation of gas permeability in hydrate-bearing sediments experimentally. They found that permeability depends on initial water saturation in the samples and the fraction of pore water that is converted to hydrate.

In this research, the variation of relative permeability of carbon dioxide was measured at 20ºC and under the hydrate conditions to study the influence of the formation of gas hydrate at residual water saturation on the relative permeability.

3.6. References

Chuvilin, E., Grebenkin, S., & Tkacheva, E. (2014). Change of gas permeability of gas-saturated sediments during hydrate formation and freezing.

Chuvilin, E. M., & Grebenkin, S. I. (2015). Gas permeability variation in gas-filled soils upon hydrate formation and freezing: an experiment study.

Engler, T. W., (2010). Fluid flow in porous media.

Johnson, A., Patil, S., & Dandekar, A. (2011). Experimental investigation of gas-water relative permeability for gas-hydrate-bearing sediments from the Mount Elbert Gas Hydrate Stratigraphic Test Well, Alaska North Slope. *Marine and petroleum geology*, *28*(2), 419-426.

Jaiswal, N. J., Westervelt, J. V., Patil, S. L., Dandekar, A. Y., Nanchary, N. R., Tsunemori, P., & Hunter, R. B. (2004). Phase behavior and relative permeability of gas-water-hydrate system. In *AAPG Hedberg Conference on Gas Hydrates: Energy Resource Potential and Associated Geologic Hazards* (pp. 1-4).

Kantzas, A., Bryan., B, Taheri, S. (2017). Foundations of fluid flow in porous media.

Levine, J. (2011). Relative permeability experiments of carbon dioxide displacing brine and their implications for carbon sequestration. Columbia university.

Nimblett, J., & Ruppel, C. (2003). Permeability evolution during the formation of gas hydrates in marine sediments. *Journal of Geophysical Research: Solid Earth*, *108*(B9).

Chapter 4 Experimental Methods

4.1. Core Flooding System (CFS)

The experiments in this investigation were performed using a core flooding system (CFS), which will be described in detail in this chapter. The CFS allows the measurement of permeability of core samples before hydrate formation and during hydrate formation. Physical characteristics also need to be determined for each prepared core sample, including porosity, density and water content.

The core flooding system is designed to conduct tests on core samples to help reservoir engineers to simulate reservoir conditions for determining the permeability and residual oil or water content. Pore pressure and confining pressure can be adjusted up to 10000 psi. Figure 4.1 shows a three-dimensional image of the entire core flooding system. The main part of the system is housed inside an oven that is set atop a cart (left side of Figure 4.1). The system also has two sets of piston pumps, which are mounted on two separate carts (right side of Figure 4.1). Figure 4.2 shows the parts comprising the main unit (oven).

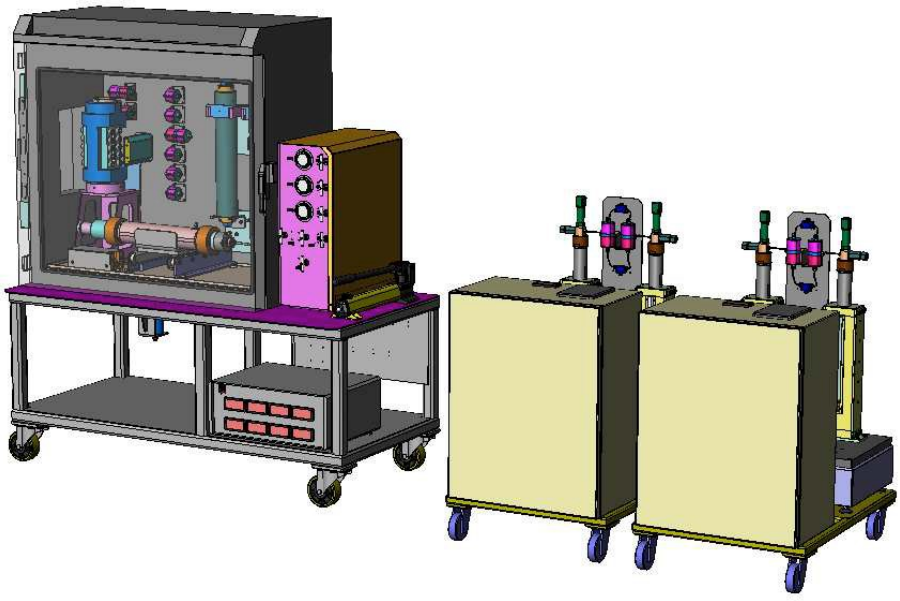

Fig. 4.1: Core flooding system (Vinci Technologies – User guide V1.1).

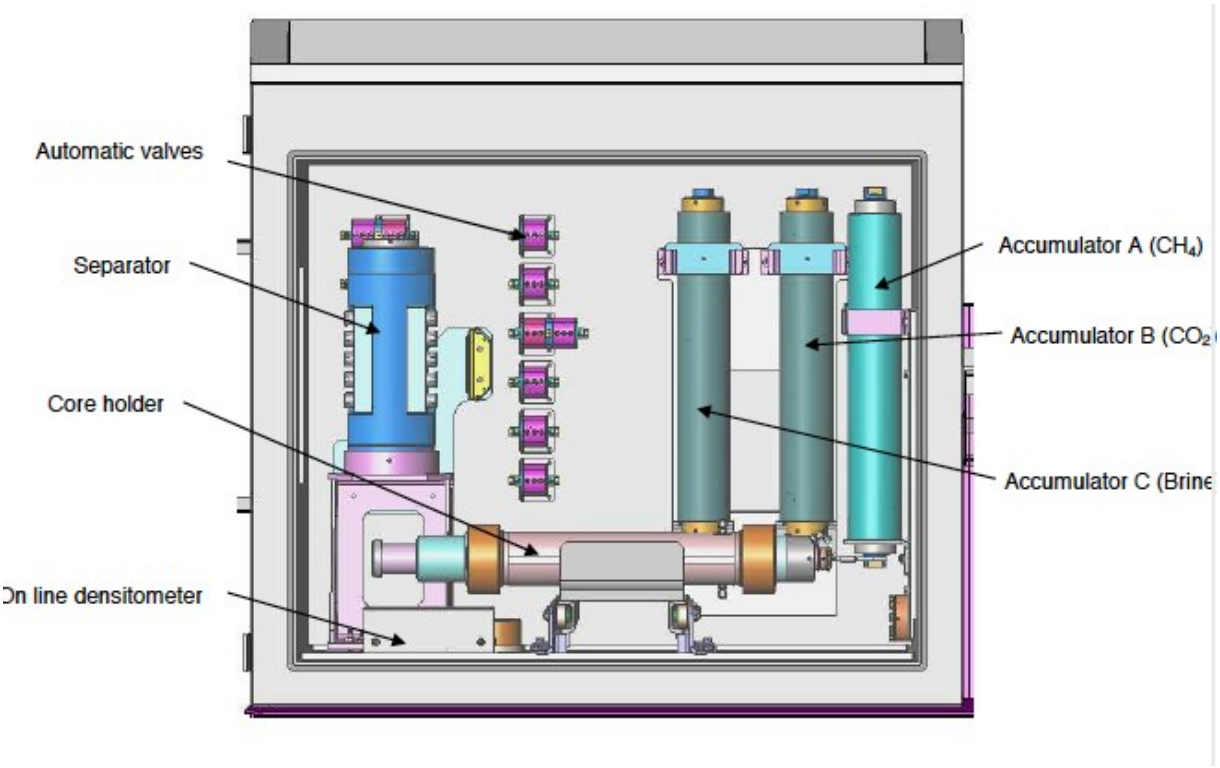

Fig. 4.2: Oven compounds (Vinci Technologies, Core flooding system – User guide V1.1).

4.2. System Overview

Water and carbon dioxide can be injected from the accumulators to the piping system. The accumulators maintain the test fluid at the desired conditions. The accumulators are cylinders equipped with two end plugs and one floating piston that separates the cylinder into a driving chamber and a test chamber. The driving chamber contains silicon oil injected from the piston pumps that control the volumetric flow rate, and the test chamber contains the test fluids. The system provides two dual-pumps (to inject water and CO_2 into the rock sample) and a set of automatic valves. The core sample was wrapped in a rubber sleeve that is placed inside the core holder. A manually operated piston pump is used to inject silicon oil around rubber sleeve to create confining pressure and to prevent fluid bypass around the core. It is important to note that confining pressure must be at least 500 psi higher than core pressure to prevent bypass. The system also contains a backpressure regulator (BPR) under the main unit to maintain a fixed downstream pressure in the core of whatever pressure that is applied to its dome, typically 150-200 psi

in this study. The BPR is designed to operate using nitrogen gas as the compressed gas in the dome and test fluid (oil, gas, water) in the body. The effluent fluid is received in the separator. The amount of displaced water entering the separator can be measured by tracking the liquid level with a video camera.

4.3. Materials

Wallace sandstone core samples, obtained from Wallace Quarries, Nova Scotia, Canada, were used in this study.

Five cores were prepared to be approximately 3.8 cm (1.5") in diameter and 15.24 cm (6") in length (as shown in Figure 4.3). They were used for measuring the relative permeability of carbon dioxide-water system before and after hydrate formation.

Deionized water was used in this study instead of brine water in order to minimize the possibility of physical rearrangement of the core networks due to any precipitation of minerals that may have an effect on the permeability measurements before and after hydrate formation.

Carbon dioxide gas with purity of 99.5% was used in this experimental study, and it was injected directly from a CO_2 cylinder that was fitted with a CO_2 pressure regulator.

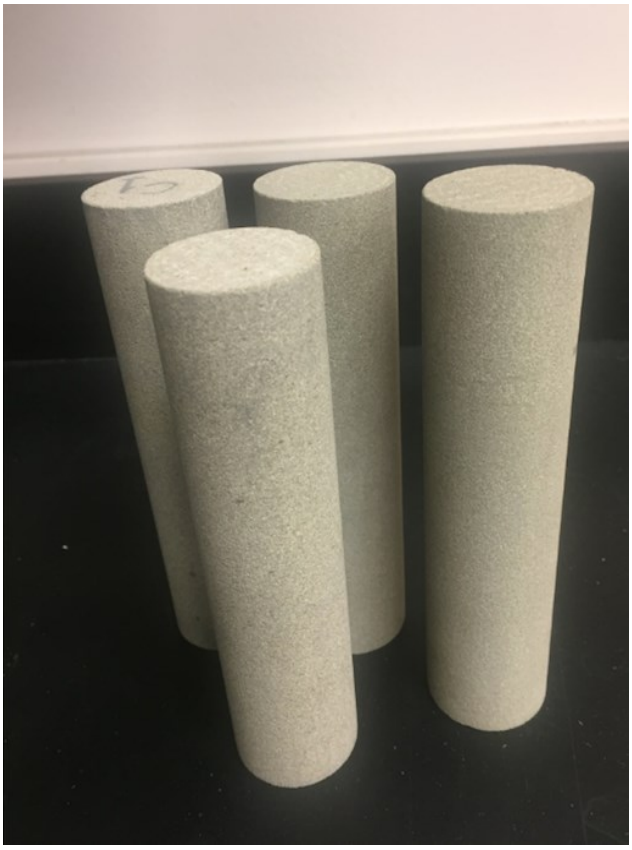

Fig. 4.3: Wallace sandstone core samples**.**

4.4. Experimental Procedure

All gas permeability measurements and hydrate formation experiments in porous media were done according to the procedure described below.

4.4.1. Core Preparation

The originally fluids present in the cores were removed by completing a thorough cleaning procedure. The first step was to soak the cores in methanol for 24 hours in a vacuum chamber to dissolve any residual oil. The samples were then placed in a fume hood and allowed to dry. After that, the samples were saturated with deionized water for 24 hours. The cores were then dried in an oven at 80ºC. Following the drying process, the dry weight of the core was measured. The last step was to saturate the cores again with water, and to measure their saturated weight.

4.4.2. Porosity Determination

Porosity, ϕ, is one of the most important properties of porous media, and it can be defined as the fraction of available void space to the total volume of the porous media. The porosity of a rock is a measure of its ability to hold the fluid. According to Nimmo (2004), there are many factors that affect the porosity of a rock core, including the shape of the particles, density, breadth of the particle size distribution and cementing.

To measure porosity in the lab, initially the dry weight of cores was measured by using a balance with a precision of 0.001 g. Then, the cores were soaked in deionized water and placed in a vacuum chamber at a vacuum pressure of -25 in-Hg. After 24 hours, the saturated cores were taken out of the vacuum chamber and their weights were measured.

Porosity can be measured by dividing the volume of water that is contained in the saturated sample (pore volume) to the total volume of the sample (bulk volume). Pore volume can be calculated by dividing the mass difference between saturated sample (M_{wet}) and dry sample (M_{dry}) to the density of the water (1 g/cm^3).

$$\phi = \frac{V_p}{V_b} \tag{4.1}$$

$$V_p = \frac{M_{wet} - M_{dry}}{\rho_{water}} \tag{4.2}$$

$$V_b = \frac{\pi D^2}{4} * L \tag{4.3}$$

where V_p is the pore volume, and V_b is the bulk volume, D = 3.8 cm, and L= 15.24 cm.

4.4.3. Monophasic Permeability Measurements

Each set of experiments started by measuring the water permeability of the core sample (one phase displacement). First, the core sample was saturated with water by placing the core in distilled water in a vacuum chamber for 24 hours to remove trapped air from the pore spaces and replace them with water. Then, the first sample was placed in the core holder. Radial and axial stress was applied on the rubber sleeve by pumping silicon oil into the core holder. Typically, confining pressure was set 2000 and 2500 psi for radial and axial pressure respectively. The backpressure regulator was typically set for monophasic permeability measurement at 150 psi.

The water permeability measurements were made by injecting water at a constant flow rate, normally between 0.5 and 1 cm^3/min into the saturated core until the outlet pressure had reached the set point for the backpressure regulator. This step was done for each set of experiments to create pore pressure in the core. Then, the automatic program for monophasic permeability testing was ready to be run. The permeability was determined by measuring the relationship between flow rate and pressure drop. This relationship was obtained automatically by allowing the system to successively increase the flow rate, allowing the pressure drop to stabilize, and then recording the data point. Once a stabilized flow rate was reached the permeability was estimated by applying the incompressible form of Darcy's law.

4.4.4. Measuring Relative Permeability of CO_2 at Residual Water Saturation

Steady state effective permeability tests were performed to measure the relative permeability of CO_2 displacing water in each rock core sample. The cores were saturated fully with water by placing them in water within a vacuum chamber. For each experiment, the back pressure was varied from 180 to 190 psi. A manual piston pump was used to set the axial and radial confining pressures to be 2500 psi and 2000 psi respectively. Then, water was introduced to the core at flow rate ranges between 0.5 and 1 cm^3/min until the outlet end core pressure reached the backpressure setpoint value. Before starting the injection of carbon dioxide, the volume of the water in the separator was calibrated to permit measurement of the amount of water displaced from the rock sample. After creating pore pressure, carbon dioxide gas was injected into the core

sample at a pressure of approximately 250 psi. After several minutes, carbon dioxide started to push the water out of the core. Displaced water flowed through the pipe to the separator and the water level in the separator was observed by video tracking on the computer. While carbon dioxide displaces the water from the core, the water saturation throughout the core decreases monotonically from inlet to outlet.

At endpoint saturation, the first step of the experiment was considered to be finished. Endpoint saturation is reached when no more displaced water reaches the separator. At this point, the steady state flow rate of the gas was measured at different injection pressures. The experiment continued by increasing inlet pressure of the gas and measuring the outlet flow rate in the separator. This step was done by opening the bottom valve of separator and observing the volume change of water due to accumulation carbon dioxide gas in separator. Once the volume changes in the separator had been determined as a function of time, the outlet flow rate of the gas at steady state could be determined by fitting a line to this data (see Figure 4.4). The effective permeability was calculated by fitting the slope of mass flow rate and integral value (see equation 3.13). Mass flow rate was calculated by multiplying volumetric flow rate by the density that was determined at the outlet pressure.

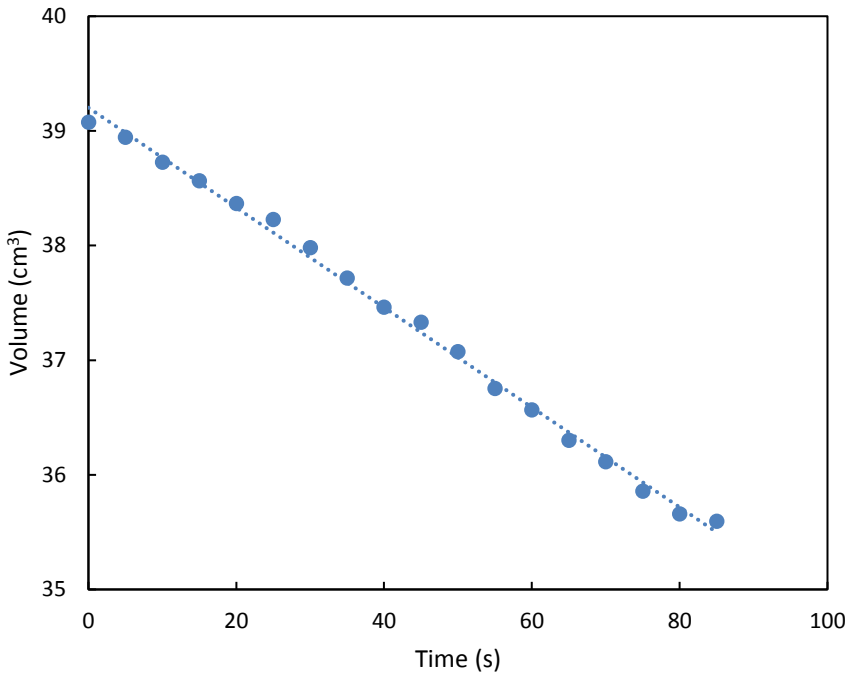

Fig. 4.4: Experimental data determination of the volume change in separator as function of time for C4 at injection pressure 250 psi.

Relative permeability experiments at residual water saturation can take a relatively long time. The length of the experiment depends essentially on the base permeability of the cores. So, the displacement process takes less time in the cores with high permeability compared to cores with low permeability.

4.4.5. Permeability Evolution in Wallace Cores Due to Injection of CO_2 Gas

The monophasic permeability and porosity measurements were repeated again after flooding with carbon dioxide at lab temperature. This step would be useful to see whether flooding CO_2 gas in the cores can cause changes in base permeability and porosity. Any new alterations would be considered during relative permeability calculation under hydrate forming conditions.

4.4.6. Hydrate formation at residual water saturation and relative permeability measurement

The last step in the experimental procedure was to measure permeability under hydrate forming conditions. Initially, the core was completely saturated with water and installed inside the core holder. Confining pressure and back pressure were set at the same values that were listed in previous procedure (approximately 2000-2500 psi as confining pressure and 170-190 psi as backpressure). Pore pressure was increased until the outlet pressure reached the value of back pressure. This step was done by flowing water through the core until the desired pressure was reached and stabilized. Then, carbon dioxide gas was injected into the core at a pressure of 250 psi (this value would be the first point of P_1) until desired water saturation was established (residual water content 14 to 30 vol%). The amount of displaced water due to CO_2 injection was estimated and used to determine the water saturation in the core. After that, the core holder and injection pipes were cooled until the desired temperature had been reached. To perform this step, the system was modified to accommodate cooling coils around the core holder and injection tubes. There were also two thermocouples connected on the core holder to measure the temperature. During the cooling process, the gas was still injected into the core to maintain pore pressure. The gas hydrate formation process is initiated, as the pressure and temperature move closer to gas hydrate equilibrium conditions. Under hydrate forming conditions, the core clearly consists of only three phases at any time. Carbon dioxide forms the gas phase, water represents the liquid phase, and gas hydrates forms the solid phase (Jaiswal, 2004). The outlet flow rate of CO_2 was measured at steady state. Also, the pressure at both ends of the core were monitored using the pressure gauges. These measurements were recorded as the first point. The experiment continued by injecting more CO_2 until the desired pressure was reached and the outlet flow rate was determining at each injection pressure (appendix A contains the experimental data that show how much P_1 was increased during each experiment under hydrate forming conditions). Finally, the relative permeability was determined by using the relationship between flow rate and pressure at different injection pressures according to the modified Darcy's law equation.

Determining the outlet flow rate of CO_2, while theoretically simple, was practically quite difficult to be performed. It was observed that hydrate sometimes formed in such a way that measurement of the resulting permeability was not possible. At high hydrate saturation, the outlet flow rate of gas was extremely low. Therefore, the back-pressure regulator was not able to act to allow measuring the gas flow rate. To mitigate this kind of problem it was decided first, to displace more water by injecting gas until residual water saturation was reached before starting cooling to avoid high hydrate saturation. Second, the cooling was started at low a pressure, and the CO_2 injection flow rate was gradually increased to avoid complete hydrate blockage, which would prevent measurement of the permeability. The experiment was considered to be finished when the gas was not able to flow through the pores at high injection pressure (600 psi) and this was considered the final measurement point.

The experimental conditions (pressure and temperature) were chosen in this study based on phase diagram of carbon dioxide hydrate (see Figure 2.2) with consideration to avoid ice formation and to allow the experiments to be performed at different injection pressures without forming of liquid CO_2.

Permeability reduction confirmed the formation of gas hydrate. Also, increasing the temperature of the system above the gas hydrate dissociation temperature at the end of the experiment produced high flow rates of the gas through the core, further confirming of the formation of the hydrate.

4.5. Uncertainty and Equipment Error

All reading and data taken by using equipment are subject to uncertainty. In this study, recording pressure values was one of the important measured data. The system provides with pressure transducers (ESI gauge-pressure transducers) with an accuracy of ± 0.1% of full scale. The equipment has a full scale of 10000 psi (700 bars). In addition, the volume of water change in separator was recorded with precision of ± 0.0005 cm^3.

4.6. References

Jaiswal, N. J., Westervelt, J. V., Patil, S. L., Dandekar, A. Y., Nanchary, N. R., Tsunemori, P., & Hunter, R. B. (2004). Phase behavior and relative permeability of

gas-water-hydrate system. In *AAPG Hedberg Conference on Gas Hydrates: Energy Resource Potential and Associated Geologic Hazards* (pp. 1-4).

Nimmo, J.R. (2004). Porosity and pore size distribution. *Encyclopedia of Soils in the Environment*, 3, 295-303

Vinci Technologies, Core flooding system – User guide Version 1.1. France.

Chapter 5 Results and Discussion – Flooding under Non-Hydrate Forming Conditions

This chapter contains the results that were collected for experiments performed under non hydrate forming conditions and the results are presented in the order in which the experiments were performed. This order also matches the order in which the experimental procedures were described in the previous chapter.

5.1. Core Characterization

A series of flooding experiments were performed on cores of Wallace sandstone after cleaning them to remove any residual contaminants. The pore volume, V_p, and porosity were determined for the selected cores. Table 5.1 summarizes the properties of the cores.

Table 5.1. Core characterization.

Sample	L (mm)	V_p (cm^3)	Porosity %
C1	152.4	21.3	12.22
C3	152.4	19.75	11.28
C4	152.4	20.92	12.15
C5	152.4	20.09	11.62
C6	152.4	20.75	11.9

5.2. Monophasic Permeability

The water monophasic permeability experiments were performed at the beginning of the study for all the core samples. The experiments were run at conditions of room temperature (20ºC) and backpressures between 150 and 200 psi. The monophasic permeability was calculated using the incompressible form of Darcy's law. The

permeability was determined from the slope of the linear relationship between volumetric flow rate, Q, and pressure drop, ΔP. Figures 5.1, 5.2, and 5.3 show the experimental data for measuring monophasic permeability for cores C1, C3 and C4 respectively. Appendix A contains the recorded experimental data for all five cores

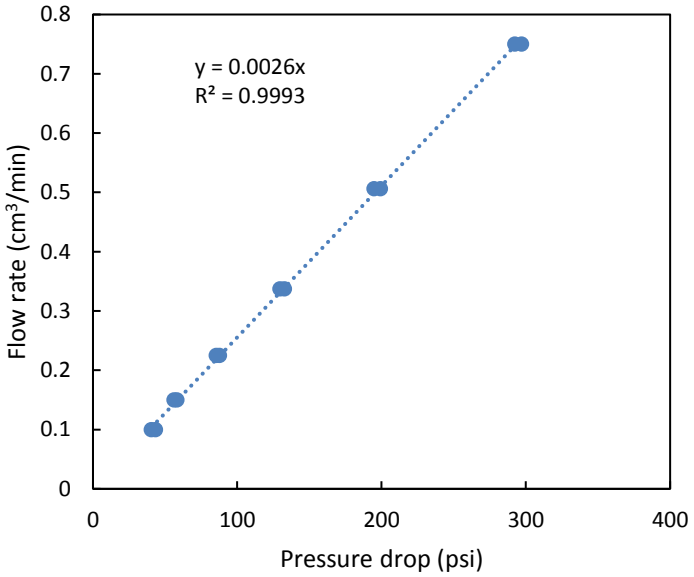

Fig. 5.1: Experimental determination of monophasic permeability for C1.

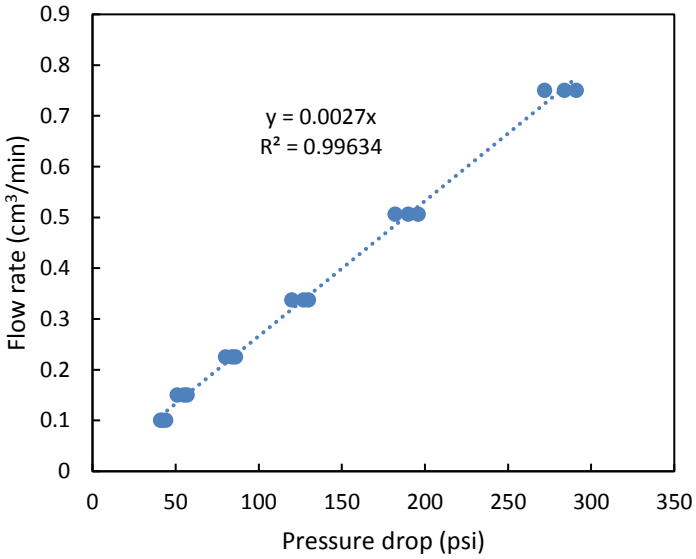

Fig. 5.2: Experimental determination of monophasic permeability for C3.

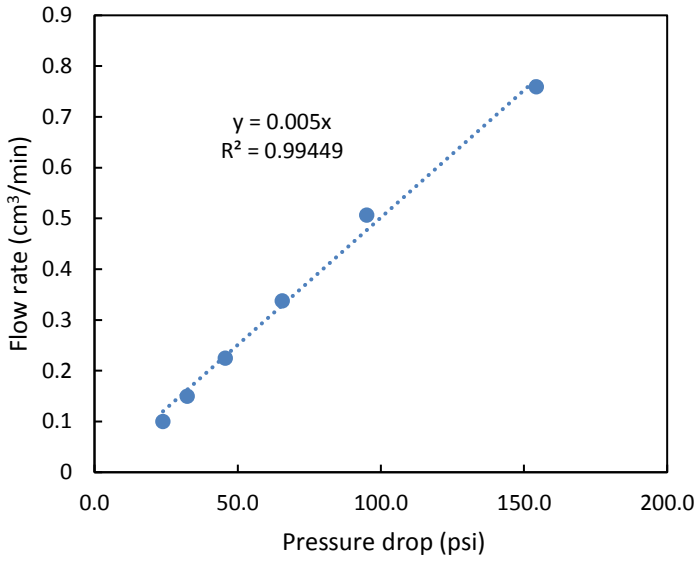

Fig. 5.3: Experimental determination for monophasic permeability for C4.

The results show that monophasic permeability of the Wallace cores samples ranges from 0.46 mD to 1.63 mD. The calculated permeability of each core from repeated experiments is shown in Table 5.2.

Table 5.2. Properties and measured base permeability (*K*) of selected cores**.**

Sample	**Length (mm)**	**Porosity**	***K* (mD) (±0.005 mD)**
C1	152.4	12.22	0.85
C3	148.3	11.71	0.88
C4	152.4	12.15	1.63
C5	152.4	11.62	0.91
C6	152.4	11.9	0.46

5.3. Relative Permeability

The relative permeability of carbon dioxide in the core samples at residual water saturation was experimentally determined using modified Darcy's law. At irreducible water saturation, mass flowrate of carbon dioxide was measured at different injection pressures. Relative permeability was determined from the slope of a plot of mass flow rate *vs.* the integral value (Equation 3.13) at 20ºC. Figures 5.4, 5.5, and 5.6 show the linear relationship of mass flow rate and integral value for C1, C3, and C4 respectively. It was found that K_r ranges from 0.089 mD to 0.139 mD. Table 5.3 summarizes the relative permeability values for tested cores and experimental data is contained in Appendix A.

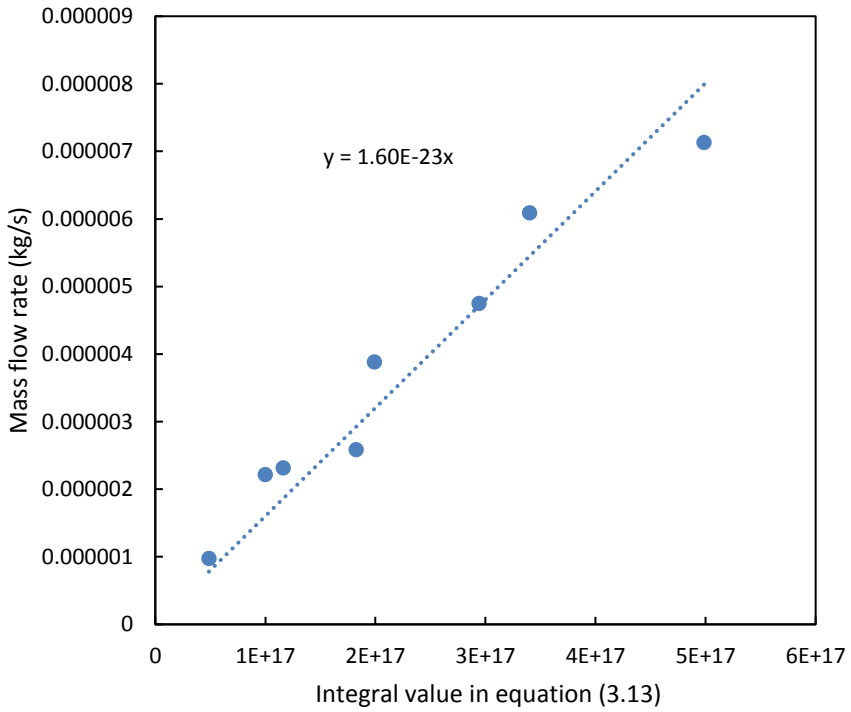

Fig. 5.4: Experimental determination of CO_2 relative permeability for sample C1.

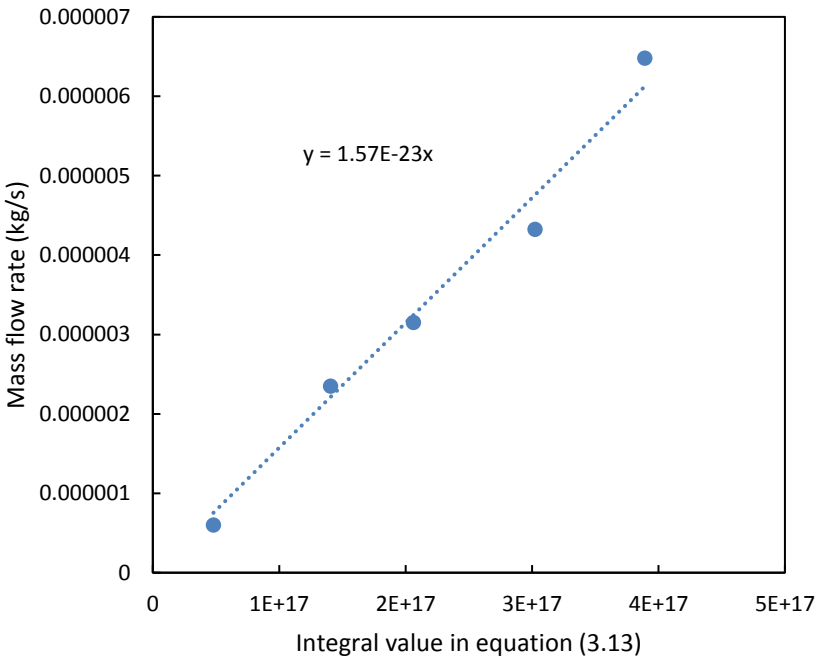

Fig. 5.5: Experimental determination of CO_2 relative permeability for sample C3.

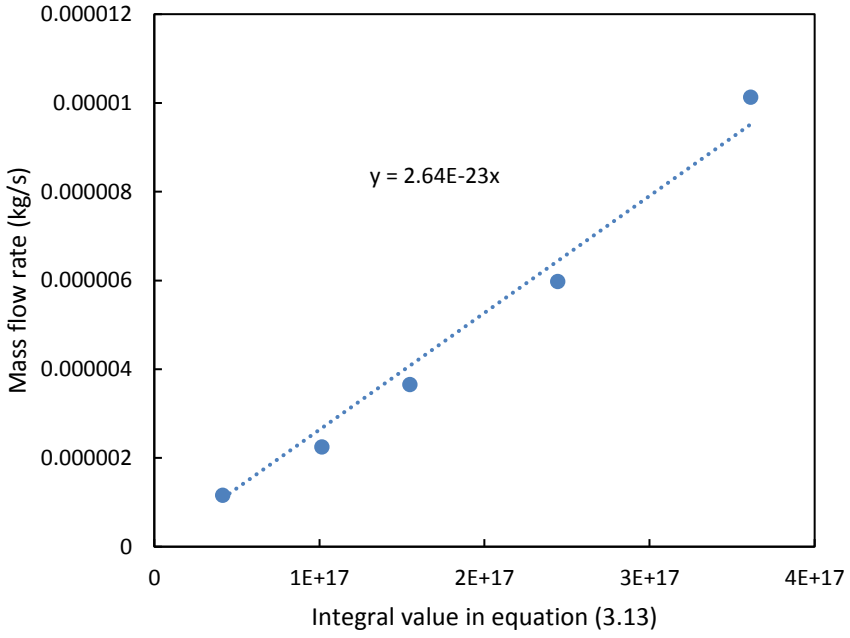

Fig. 5.6: Experimental determination of CO_2 relative permeability for C4**.**

Table 5.3. Measured relative permeability for tested cores

Sample	K_a (mD) (±0.005 mD)	K_{eff} (mD) (±0.0005 mD)	K_r (±0.0005 mD)
C1	0.85	0.118	0.139
C3	0.88	0.116	0.132
C4	1.63	0.193	0.118
C5	0.91	0.078	0.089
C6	0.46	0.061	0.134

5.4. Permeability Evolution in Wallace Cores Due to Injection of CO_2 Gas

In this study, the monophasic permeability and porosity of the cores was measured again after injection of CO_2 gas at 20ºC to see whether CO_2 gas affected rock core properties. It was found that there was an increase in both permeability and porosity for most of the cores. In general, there was an increase in permeability due to injection of CO_2 by approximately 26% for the samples C1, C3 and 9.8%for C4, while C5 and C6 did not show any significant change in permeability. The overall change in porosity ranges between 1.3% to 4.6%. Table 4.4 summarize the changes of the rock properties before and after flooding CO_2.

Table 5.4. Porosity and permeability change due to CO_2 flooding

Wallace samples	Porosity before flooding	Porosity after flooding	Permeability before flooding (mD)	Permeability after flooding (mD)	Permeability change %
C1	12.22	12.6	0.85	1.11	30.5
C3	11.28	12.25	0.88	1.07	21.5
C4	12.15	12.6	1.63	1.79	9.8
C5	11.62	11.78	0.91	0.88	-3.2
C6	11.9	12.31	0.46	0.44	-2.1

5.5. Calculation of monophasic permeability and relative permeability at 20°C

In this section, an example will be presented to show the calculation of the base and relative permeability for the sample C5

Test conditions

Sample number	**C5**
Diameter	38 mm
Length	152.4 mm
Surface area	11.34 cm^2
Pore volume	20.09 cm^3
Bulk volume	173.75 cm^3
M_{dry}	409.10 g
M_{wet}	429.19 g
Porosity%	11.62
Axial pressure	2500 psi
Back pressure	150 psi
Radial pressure	2000 psi

Monophasic permeability calculation

The incompressible form of Darcy's law (see equation 3.1) was applied to calculate K_a. once stabilized flow rate was noted at constant differential pressure. Appendix A provides the recorded values of Q *vs.* ΔP for sample C5.

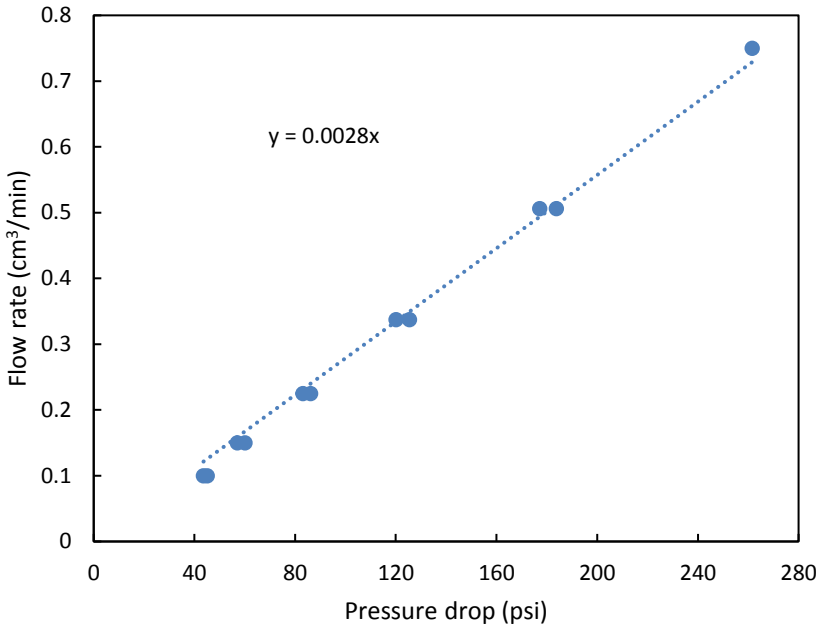

Fig. 5.7: Experimental determination for monophasic permeability for C5.

Figure (5.7) represents the linear relation between Q and ΔP for C5. Darcy's law can be applied to calculate K_a by substituting the slope ($KA/\mu L$) with 0.0028 (cm^3/(min psi)), which equals in SI unit 7.01×10^{-15} (m^3/(s Pa)). K_a is calculated as the following:

$$K_a = 7.01 \times 10^{-15} \left(\frac{\mathrm{m}^3}{\mathrm{sec}\,.\,\mathrm{Pa}}\right) \times\ 0.1524\ (m) * \frac{0.001\left(\frac{\mathrm{kg}}{\mathrm{m}\,.\,\mathrm{sec}}\right)}{11.39 \times 10^{-4}(m^2)} * 10^{15}\,\frac{\mathrm{mD}}{\mathrm{m}^3}$$

$$K_a = 0.91\ \mathrm{mD}$$

Relative Permeability Calculation

The relative permeability was determined at 20ºC by applying the modified form of Darcy's law at 20ºC.

$$mL = -\frac{KA}{RT}\int_{P_2}^{P_1} \frac{PdP}{-2.4460E-12P^2 - 2.6590E-9P + 1.4252E-05} \qquad (5.1)$$

Table 5.5 shows the experimental data that was collected during the experiment to determine relative permeability at residual water saturation for C5. Mass flow rate was estimated by multiplying the density of carbon dioxide (at P_2) by the measured outlet flow rate (Q_o). Figure 5.9 shows the relation between the mass flow rate and $\int\frac{PdP}{\mu Z(P)}$ that evaluated numerically by using the trapezoid rule.

Table 5.5. Experimental data used to calculate relative permeability for C5

P1 **(psi)**	***P2*** **(psi)**	***m*** **(g/min)**	***Integral value in equation*** **(5.1)**
284	178	0.0432	8.629E+17
337	178	0.09168	1.456E+17
416	180	0.1744	2.540E+17
481	178	0.2244	3.655E+17

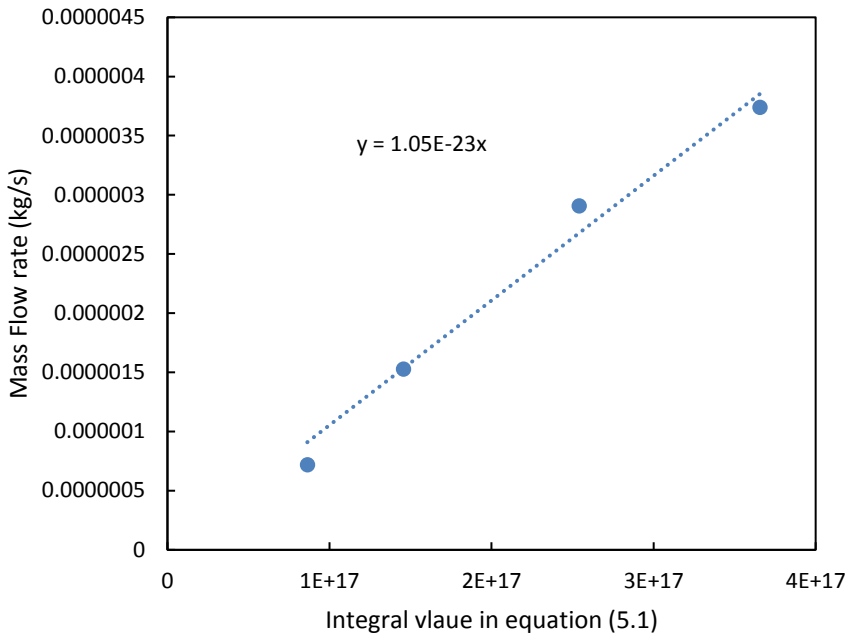

Fig. 5.8: Experimental determination to measure relative permeability for C5.

From the experimental data as shown in Figure 5.8, the slope was used in the modified form of Darcy's law with K_a = 0.912 mD, T = 293 K and, R = 8314 Pa m^3 $kmol^{-1}$ K^{-1}. Substituting all previous variables into equation 5.1, K_r was calculated to be 0.085 mD for the sample C5.

5.6. General Discussion

It was expected in this study that water monophasic permeability values would be in the same range for all rock cores. It was assumed prior to the experiments that the physical properties of the Wallace sandstone reservoir would be relatively uniform and homogeneous. However, the data show that the measured monophasic permeability of cores C6 and C4 (0.46 mD and 1.63 mD respectively) are not similar to the rest of the cores, which had permeability values in the range of 0.85 to 0.91 mD. The differences in permeability might have been due to drilling C4 and C6 from a portion of the reservoir that has been exposed to the different geochemical conditions of pressure and temperature that caused permeability alteration. Also, dissolution of feldspar and clay formation may have an effect on the surface chemistry of the rock. So, knowing the history of reservoir can determine the quality of the reservoir rock properties.

The endpoint relative permeability was measured for selected cores. The data show that the measured endpoint relative permeability is relatively low, with the K_{ri} values ranging from 0.089 to 0.139. Actually, it was expected that CO_2 gas would behave as a strongly non-wetting phase. As a result of being a strongly non-wetting phase, it was assumed prior to the experiments that the relative permeability measurement of CO_2 displacing water would be high, likely in the range of 0.8 to 1 (Levine, 2011). As was explained in Chapter 3, a strongly non-wetting phase has the ability to access the most permeable and the largest pathways, resulting in high relative permeability. Instead, the experimental result shows low permeability values, clustered around 0.089 to 0.139 mD. This result could be caused by variation of initial water saturation and wettability state of the cores. Also, the variation of the final water saturation for the same core can affect the measured relative permeability (Schembre and Tang, 2006). Measured values indicate that the CO_2 behaving as a weekly non-wetting fluid.

Moreover, in this research the monophasic permeability of water in the selected Wallace sandstone samples was measured again after flooding with carbon dioxide. This step is important to consider permeability alteration due to injection of CO_2 into saturated cores to account for this effect in the calculation of the relative permeability after hydrate formation. The results show an increase in permeability by an average of 26% for C1, C3, and 9% for C4, while the rest of the cores did not show any significant change. Iglauer *et al.* (2014) explained in their research that CO_2 gas can dissolve in water to create an acidic environment. Formation of carbonic acid can create large holes that are called "wormholes" which significantly increase the permeability of the rock.

Further, the composition of the rock can determine the extent of permeability change. Sandstone usually contains a considerable quantity of clays and cement rather than quartz. These impurities usually have high reactivity in an acid environment. So dissolution and transportation of these compounds out of the core could occur, and this would cause an increase in permeability. However, sandstone also frequently contains significant amounts of quartz, which is not expected to change due to carbon dioxide injection.

The minerals analysis of the Wallace sandstone carried out by Dalhousie University (2001) found a composition of 82 wt% of silica (SiO), 8.12 wt% Aluminum oxide (Al_2O_3), 3.19 wt% ferric oxide (Fe_2O_3), 1.67 wt% sodium oxide (Na_2O), 1.13 wt% potassium oxide (K_2O), 0.72 wt% magnesium oxide (MgO), 0.81 wt% calcium oxide (CaO), 0.29 wt% titanium oxide (TiO), 0.1 wt% manganese oxide (MnO), and 2.59wt% loss on ignition. Appendix B shows the chemical analysis document published by Wallace Quarries Limited. According to mineral analysis, the change in permeability may be from the result of the transport some of these minerals, even if they represent small percentage.

5.7. Conclusions

Wallace sandstone cores were used to perform experiments in a core flooding system to measure the relative permeability of carbon dioxide displacing water at irreducible water saturation. The permeability measurements also can be called the endpoint relative permeability. The experimental results show low values of endpoint relative permeability which ranged from 0.089 to 0.139. Because wettability controls the relative permeability, this result indicates that carbon dioxide was not behaving as strongly non-wetting phase.

Additionally, in this experiment the permeability change after injection of CO_2 was determined. This was important to account for permeability alteration in the calculation of relative permeability during hydrate formation. It was found that the permeability did not change significantly for cores C5 and C6, while there was an increase in permeability for the rest of the cores by an average of 26%. The measured permeability after flooding with carbon dioxide indicates that injection of carbon dioxide into saturated rocks creates acidic environment that can impact on the permeability and pore morphology. The chemical composition of the rocks is a significant factor that controls the permeability alteration due to CO_2 injection. So, it is necessary to carefully assess the permeability and permeability change prior to CO_2 injection to avoid project failure.

5.8. References

Iglauer, S., Sarmadivaleh, M., Al-Yaseri, A., & Lebedev, M. (2014). Permeability evolution in sandstone due to injection of CO_2-saturated brine or supercritical CO 2 at reservoir conditions. *Energy Procedia*, *63*, 3051-3059.

Levine, J. (2011). Relative permeability of carbon dioxide displacing brine & their implication for carbon sequestration. Columbia University.

Schembre, J. M., Tang, G. Q., & Kovscek, A. R. (2006). Wettability alteration and oil recovery by water imbibition at elevated temperatures. *Journal of Petroleum Science and Engineering*, *52*(1), 131-148.

Chapter 6 Results and Discussion – Flooding under Hydrate-Forming Conditions

This chapter contains the results that were collected for experiments performed under hydrate forming conditions.

6.1. Core Samples

The hydrate formation experiments were performed on four selected cores. Table 6.1 summarizes the properties of the selected samples. It is important to note that there was a small change in the length of the selected samples due to small damage that occurred during the first set of experiments.

Table 6.1. Properties of the cores used for core flooding experiments under hydrate forming conditions

Sample	L (mm)	K_a (mD)
C1	149.7	0.85
C3	148.3	0.88
C4	149.8	1.63
C5	148.0	0.91

6.2. Relative Permeability During Hydrate Formation

Carbon dioxide hydrate was formed in core samples having residual water contents between 15 and 30 vol%. The displacement process was performed at temperatures of approximately 4ºC and 3ºC, and injection gas pressure starting from 250 psi. Relative permeability was calculated during hydrate formation by using the modified, compressible form of Darcy's law. In Chapter 5, this modified form of Darcy's law showed linear relationship for all experimental data between mass flow rate and integral

value in Equation 3.13 at 20ºC. However, at low temperature (under hydrate formation condition), the experimental data did not display the same linear relationship. Figure 6.1 shows the experimental data of three repeated experiments for core 4. This figure clearly displays a non-linear relationship between mass flow rate and integral value in Equation 3.12 under hydrate forming conditions especially for high pressure drops, as shown in Figure 6.2. The three repeated experiments show almost the same relationship, within an error percentage of approximately 10%.

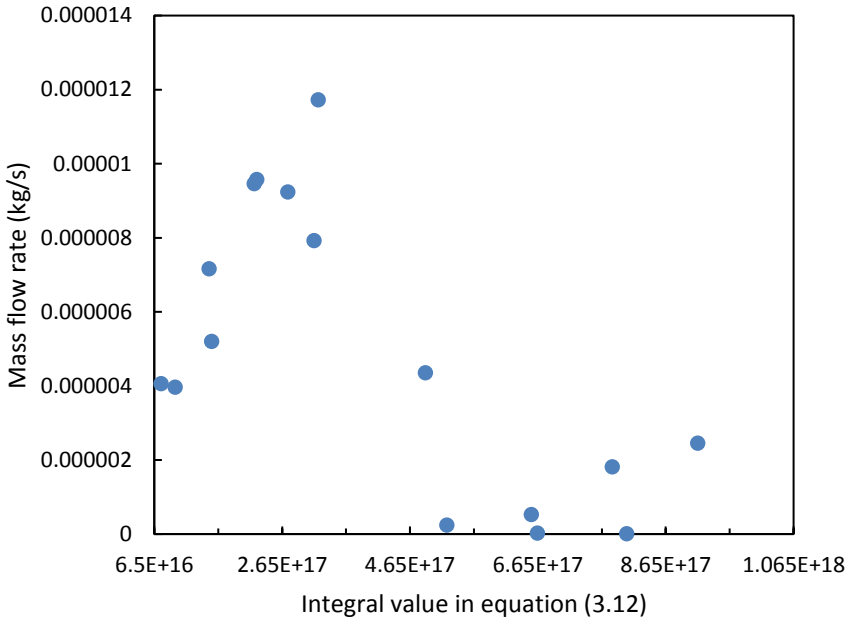

Fig. 6.1: Experimental data for three repeated CO_2 core flooding experiments for C4 at 4ºC.

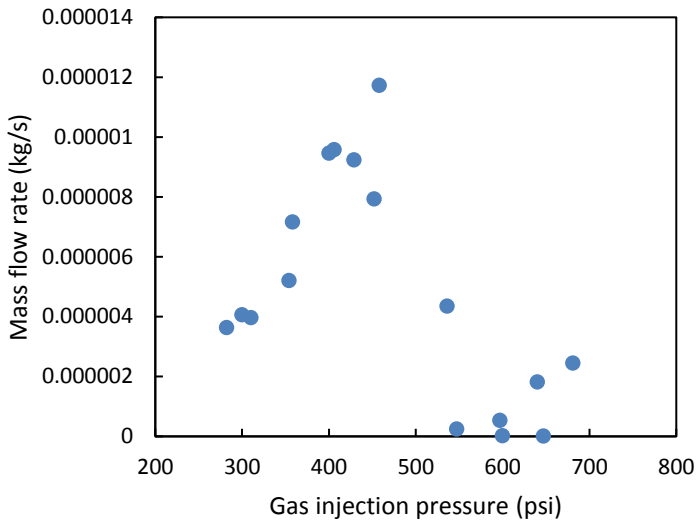

Fig. 6.2: Experimental data for three repeated experiments for C4 at 4 ºC.

Modified Darcy's law was also applied to experimental data under hydrate forming conditions for samples C3 and C1. The result exhibited a similar trend to the data for C4. Figures 6.3 and 6.4 show the relationship of mass flow rate versus gas injection pressure for C1 and C3, respectively. The experiment was repeated two times, one performed at 4°C (blue triangles dots) and the second experiment performed at 3°C (red circle dots).

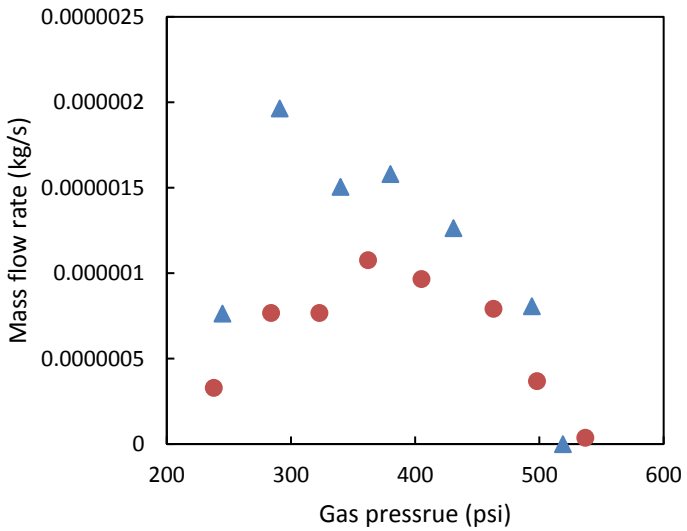

Fig. 6.3: Experimental data of mass flow rate *vs* gas injection pressure for C1 under hydrate forming conditions at 4ºC (blue triangles dots) and 3ºC (red circles dots).

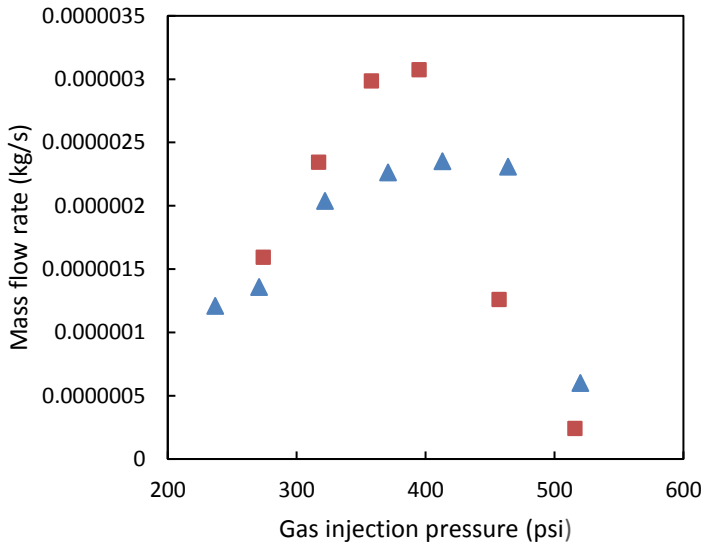

Fig. 6.4: Experimental data of mass flow rate *vs.* gas injection pressure for C3 under hydrate forming conditions at 4ºC (blue triangles dots) and 3ºC (red squares dots).

The overall results show a significant decrease in effective permeability with the increasing hydrate saturation that occurs at increasing gas injection pressures. Figure 6.5 shows variation of permeability with gas pressure drop for sample C4 for the three repeated experiments at 4ºC.

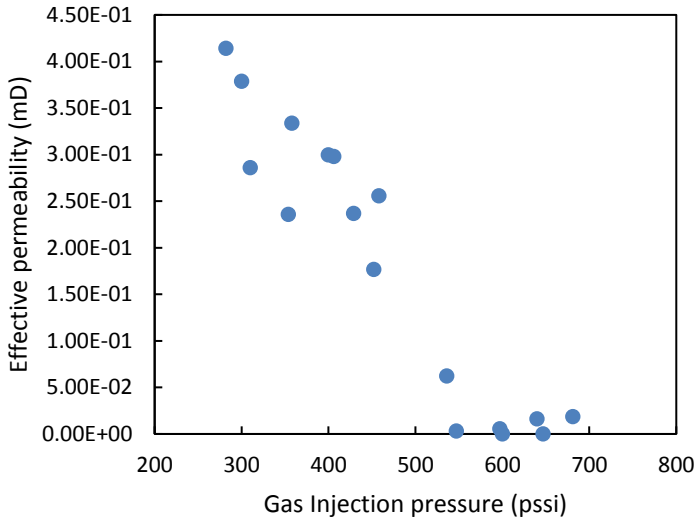

Fig. 6.5: Variation in permeability due to hydrate formation for sample C4 at 4ºC.

The next two figures show how the rate of permeability reduction is different among the cores at the same temperature. Figure 6.6 shows permeability reduction rate for samples C1, C3 and C4 at 3ºC. Conversely, Figure 6.7 displays permeability variation for samples C1, C3, C4 and C5 at 4ºC.

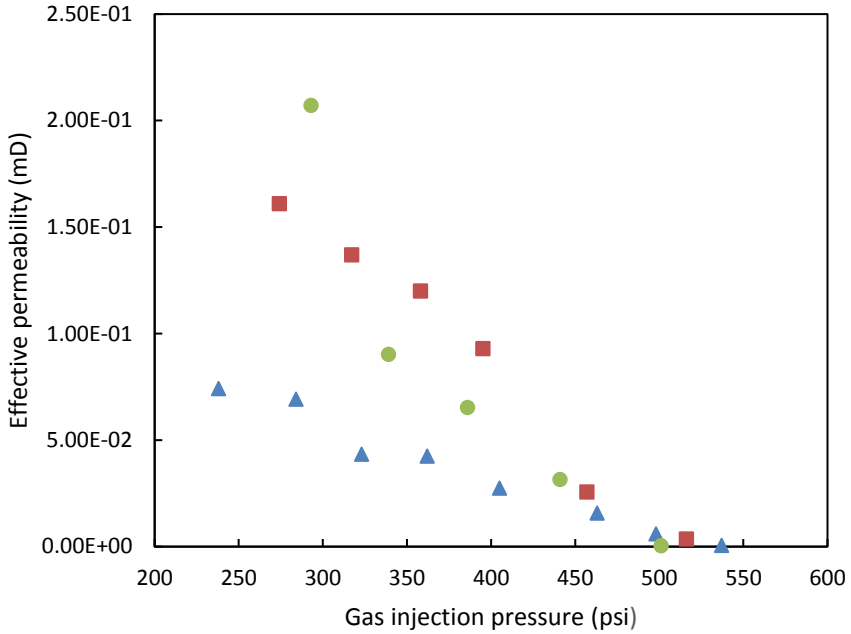

Fig. 6.6: Reduction in effective gas permeability versus gas hydrate pressure at 3ºC for tested cores (blue triangles for C1, red squares for C3, and green circles for C4). (water content was 7.90, 3.63 and 3.58 mL for C1, C3 and C4 respectively).

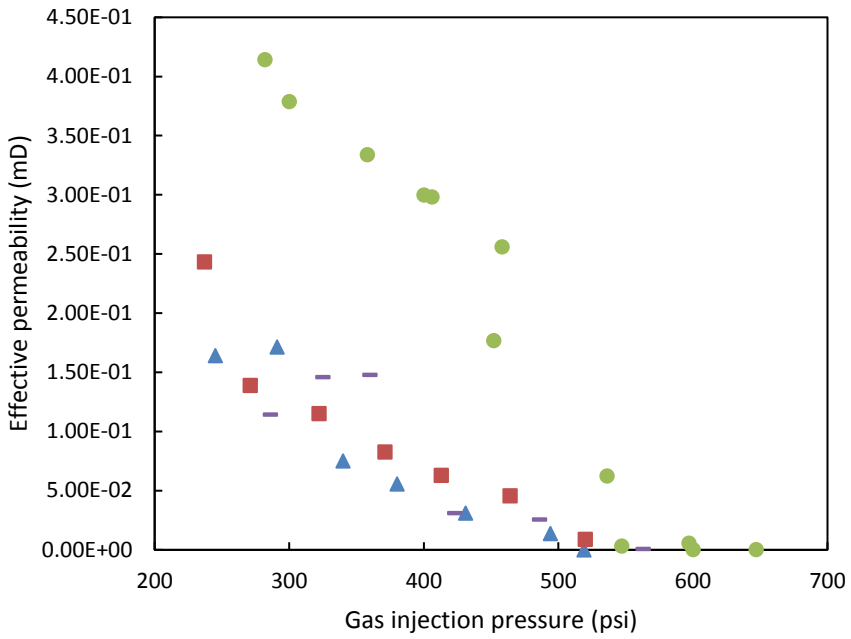

Fig. 6.7: Reduction in effective gas permeability versus gas injection pressure at 4ºC (blue triangles for C1, red squares dots for C3, green circles for C4 and, purple dash for C5). (water content was 8.46, 3.71, 2.10 and 3.5 mL for C1, C3, C4 and C5).

This study also aimed to understand the effect of temperature change on CO_2 hydrate formation rate for the same sample. This effect can be observed by looking at the permeability change in the same sample at different temperatures. Figure 6.8 illustrates. how the permeability remains constant with pressure at 20ºC for two repeated experiments and decreases when the experiments were performed at 3 and 4ºC. The reason for having two different values of effective permeability at 20ºC could be as a result of differences in final residual water saturation in the core.

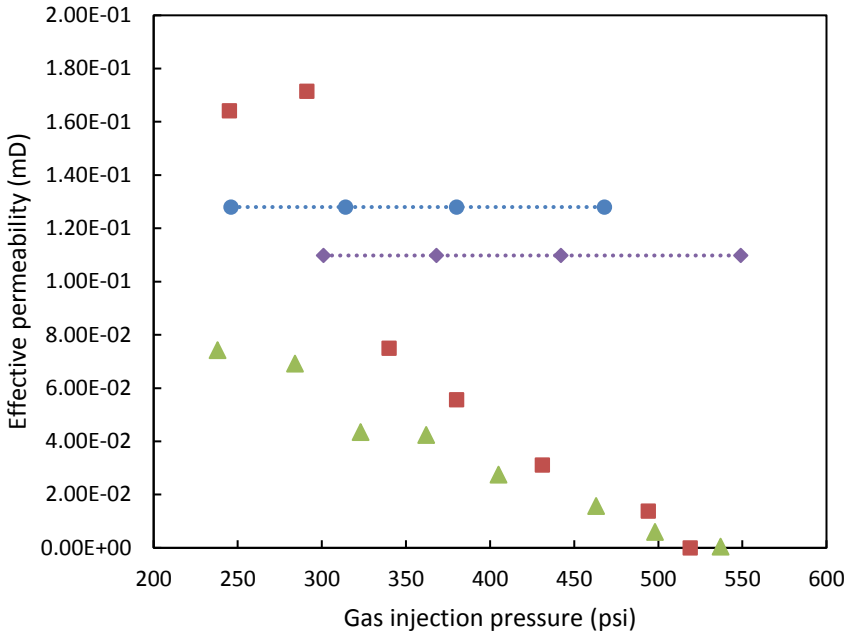

Fig. 6.8: Permeability reduction for sample C1 at 20ºC, blue circles (Exp.1) and purple diamonds (Exp.2), 4ºC (red squares) and 3ºC (green triangles).

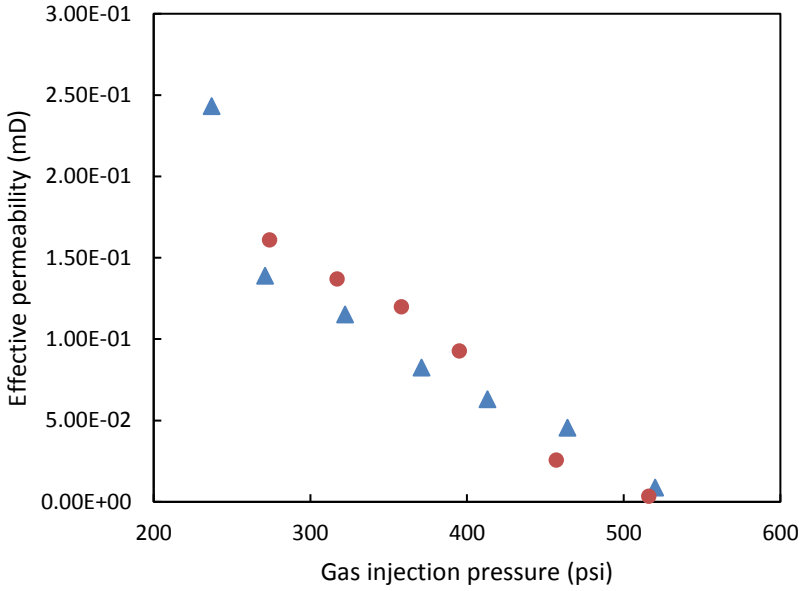

Fig. 6.9: Permeability reduction for sample C3 at 4ºC (blue triangles) and 3ºC (red circles).

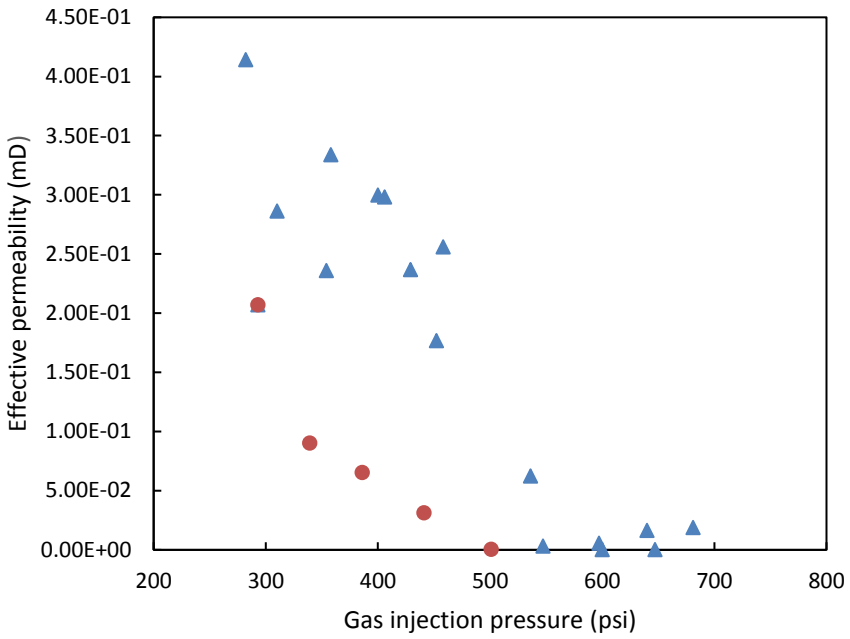

Fig.6.10: Permeability reduction for sample C4 at 4ºC (blue triangle) and 3ºC (red circles).

6.3. General Discussion

In general, the process of CO_2 injection into saturated samples of porous media involves water as wetting phase and CO_2 as non-wetting phase during the displacement process. When CO_2 gas enters the core, the water will be displaced gradually. Hydrates form during the displacement process when CO_2 gas sweeps through the pore area containing residual water with low temperature and high pressure. The saturation of CO_2 hydrate increases at increasing injection pressures. Figure 6.10 shows hydrate formation during the two-phase displacement process.

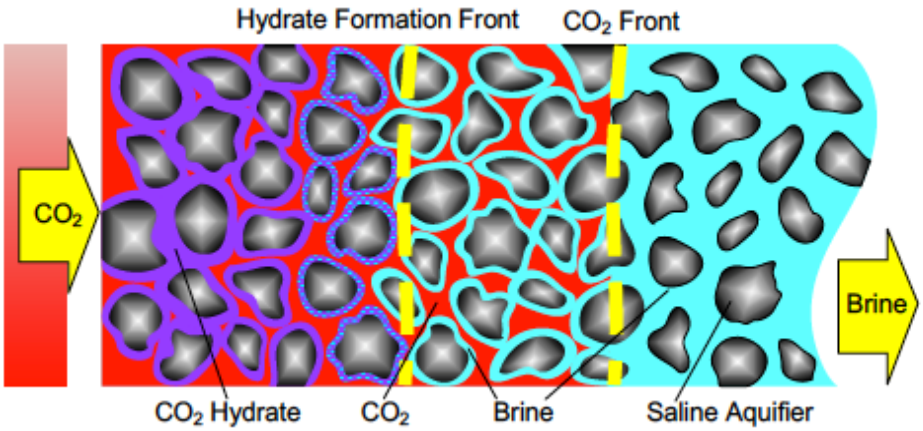

Fig. 6.11: Hydrate formation during CO_2 injection into a reservoir saturated with brine (Ding and Liu, 2014).

In this research, CO_2 hydrate was formed successfully by injecting cold CO_2 gas from a CO_2 cylinder into core samples containing residual water saturation. The cooling process of the system started after displacing most of the mobile water from the sample at 20ºC to avoid complete blockage of gas at lower injection pressure.

It was found experimentally that carbon dioxide hydrate started to form in Wallace sandstone samples when the pore pressure reached 290 psi at 3 and 4ºC. This value is matches with the hydrate forming pressure in bulk phase at the same temperature (see Figure 2.2).

At increasing CO_2 injection pressure, the quantity of formation of hydrates increases inside the porous media. However, because of difficulties to trying to visualize the hydrate growth in the porous media, the mechanism of hydrate blockage inside the pores is still not well understood. Dvokin *et al.* as cited in He (2012) claimed four possible locations for hydrate distribution in porous media. Gas hydrate may float in the pore fluid, fill pore space, surround and cement the grains or cement only grain contact. Visualizing hydrate formation directly would require very specialized, high cost equipment. However, in the experiments in this research the main purpose was to try to determine whether the hydrate growth occurs in direction of length or density. From the experimental data, it is possible to calculate the thickness of hydrate by applying Darcy's

law and assume the minimum hydrate forming pressure of 290 psi, so the length of the core that does not include hydrate can be determined by applying modified Darcy's law and using the permeability value that was estimated at 20ºC. Therefore, the length of the hydrate would be the total length minus the length without hydrate. Figure 6.12 shows the relationship between the length of hydrate growth and the pressure. The linear relationship at the start of the curve confirm that the hydrate grows in direction of length through the core. However, as gas injection pressure increases, the length is almost constant. This deviation likely means that the hydrate became denser (*i.e.,* more area was blocked).

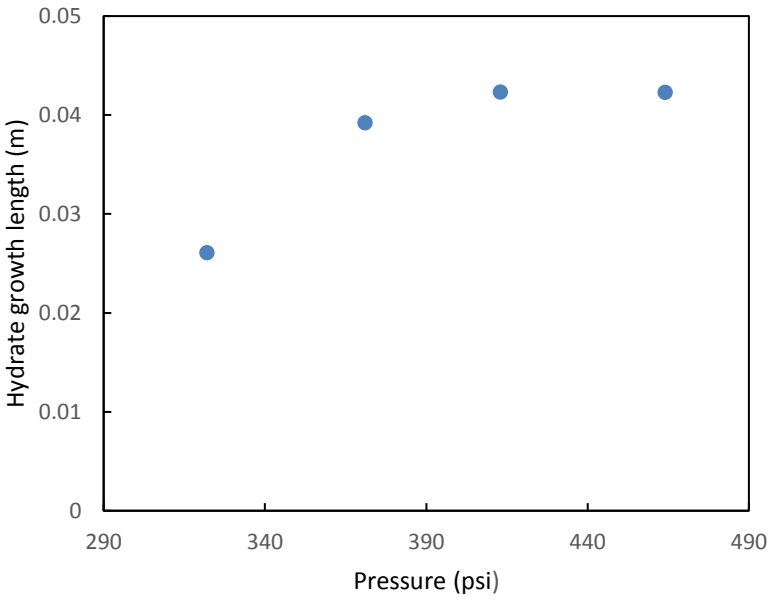

Fig. 6.12: Estimated hydrate growth length in the C3 at 4ºC with total length 0.1483 m.

It was found that the maximum length of hydrate growth represents 28.5% of the total length of the core. This ratio was estimated by dividing the maximum length of the hydrate section of the core, which is equal to 0.0423 m, to the total length of the core 0.1483 m. Figure 6.13 illustrates how the effective permeability of the gas through the hydrate layer decreases with increasing gas injection pressure. The negative value indicates that formation of hydrate in pores makes the sample completely impermeable for CO_2 flowing. The negative value also indicates that the initial assumption of uniform hydrate density in the section of the core above 290 psi is likely also not quite valid.

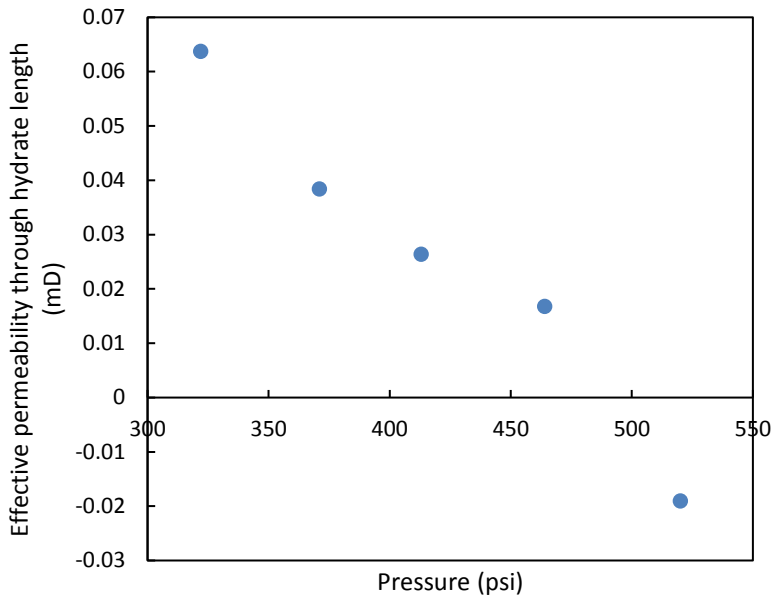

Fig. 6.13: Effective permeability of carbon dioxide during hydrate layer versus gas pressure for C3 at 4ºC.

Applying modified Darcy's law under hydrate forming conditions did not show a linear relationship between mass flow rate and the integral value of equation (3.11) and (3.12) as it showed at 20ºC (using equation 3.13). Figures 6.1 shows non-linear relationship between mass flow rate and integral value for three repeated experiments for C4 at 4ºC. Figures 6.2, 6.3 and 6.4 show the same relationship but in terms of gas injection pressure rather than integral value for C4, C1 and C3, respectively. It can be seen at low pressure drop that the relation looks linear, but at increasing pressure drop the mass flowrate decreases. The reason for this behaviour could be that the experiment started at pressures below the minimum pressure required for hydrate formation, so mass flow rate increases as the gas pressure increases. However, when the pressure drop was high enough for the gas to attack the residual water in smaller pores the hydrate started to form. As a result, the mass flow rate started to decrease as the quantity of CO_2 hydrate in the samples increased.

In addition, it was found experimentally that formation of CO_2 hydrate significantly affects the gas permeability, and increasing the quantity of hydrate inside the pores makes the samples less permeable to gas or effectively impermeable. Also, it was found that the

permeability reduction is different among cores. Figure 6.6 shows the permeability reduction for three cores at 3ºC, and it is clear that sample C1 shows the greatest permeability reduction compared to samples C3 and C4. This difference can be explained by the different water contents in the samples, so the quantity of hydrate formation was higher in the samples that contain higher water content. The data showed that the water content under hydrate forming conditions in sample C1 was 7.906 mL, while it was 3.6 and 3.58 mL for C3 and C4, respectively. However, looking at Figure 6.7, C4 (green circles) shows the lowest permeability reduction at 4ºC, because the estimated residual water in this sample was smaller compared to other cores. The residual water content in C4 at 4ºC was 2 mL, while the water content for other samples was 8.46, 3.7 and 3.65 mL for C1, C3 and C5, respectively. However, from Figure 6.7 it can be seen that the permeability reduction for C4 is quite small compared to the other cores. This deviation for C4 does not follow the same trend as the other cores, even considering the fact that C4 contained a smaller amount of water. This means that may there must be other factors that cause this deviation. By reviewing the results of monophasic permeability for the cores, it was found that the absolute permeability of C4 is the largest one (1.63 mD). So, the interconnection of the pores inside the sample can contribute to decrease the effective permeability reduction of CO_2 during hydrate formation.

To understand the effect of temperature on the gas permeability reduction during hydrate formation, the experiments were carried out at 4 and 3ºC for C1, C3 and C4. The result shows that the permeability reduction was almost the same at 4 and 3ºC for sample C3 (as shown in Figure 6.9). This means that the amount of hydrate formation is similar at these two temperatures. Meanwhile, the permeability reduction was different for C1 and C4 at these two temperature (see Figure 6.8 and Figure 6.10). The data show that the residual water saturation was almost the same in the sample C3 at 4 and 3ºC. This means that the hydrate saturation should achieve almost the same level at 3 and 4ºC. However, the residual water saturation was different at different temperatures for C4 and C1, and therefore the permeability reduction was different. This result indicates that the gas permeability reduction depends on the water content that converts to gas hydrate, and is less impacted by temperature changes.

6.4. Conclusions

A core flooding system was modified to allow the measurement of gas permeability during hydrate forming conditions. In this research, the evolution of permeability during hydrate formation was investigated. The following conclusions can be made from this study:

- Several experiments were conducted in the core flooding system and they show that it was possible to form CO_2 hydrates in the Wallace sandstone cores at 4 and 3ºC at minimum pressures of 290 psi.
- Estimation of the length of the hydrate layer in core and the effective permeability of CO_2 through the hydrate layer shows that the mechanism of hydrate growth occurs along the length of the core first and then continues growing in terms of density until completely blocking the fluid flow paths.
- Measuring conventional relative permeability of gas displacing water at normal conditions is fairly straightforward and is conducted easily. However, relative permeability measurements during gas hydrate formation within porous media is more complex because of the poorly understood mechanisms and formation conditions of CO_2 hydrate inside porous media.
- The ability to form gas hydrate in the sample while still measuring a meaningful permeability value was confirmed. The results clearly showed that hydrate formation can significantly reduce gas permeability.
- The permeability reduction depends on the water content in the samples that can convert to hydrates. High permeability reduction would be in the samples that contains high water content.
- The results show also the permeability reduction achieve the same level at 4 and 3ºC if the samples contain the same residual water saturation. This indicates that the rate of hydrate formation is almost the same at the temperature selected in this study.

6.5. References

Ding, T., & Liu, Y. (2014). Simulations and analysis of hydrate formation during CO_2 injection into cold saline aquifers. Energy Procedia, 63, 3030-3040.

He, Y. (2012). Formation of methane and carbon dioxide hydrates in bulk and in porous media. TU Delft, Delft University of Technology.

Chapter 7 Conclusions and Recommendations

7.1. Conclusions

The research presented in this thesis was mainly aimed at investigating experimentally the influence of CO_2 hydrate formation in porous media on the relative permeability. For that purpose, a core flooding system was used and modified to conduct several experiments on the five Wallace sandstones cores. Darcy's law was modified in this study to allow measuring relative permeability for compressible gas with and without hydrate conditions. In this study, it was determined that modified Darcy's law displayed a linear relationship at 20ºC, while this relation became non-linear under hydrate forming condition. The results showed significant decrease in relative permeability under hydrate conditions. It was noted that higher permeability reductions occurred in the cores that contained high amounts of residual water content.

In addition, under this study the behaviour of hydrate formation of CO_2 gas in porous media were investigated at two different temperatures of 3 and 4ºC. It was found that the CO_2 hydrate started to form when the pore pressure reached to a value above 290 psi at the selected experimental temperatures. Also, it was observed that the quantity of hydrate formation was almost the same at these selected temperatures when the core contained the same amount of residual water.

7.2. Recommendations

The following recommendations can be made for future studies:

- A greater focus on microscopic behaviour of hydrate formation in porous media is recommended for future studies. This kind of study could be done by using a system with high quality of imaging techniques to gain knowledge about hydrate growth and the way of distribution in porous media.
- Further research could be done to provide more understanding on the kinetics of gas hydrate and dissociation based on the temperature evolution due to hydrate reactions. This could be accomplished by designing a new system that allows to accommodate several thermocouples in different locations in core samples. This

kind of research is important for developing a model that represents gas hydrate formation rate.

References

Blackwell, V. (1998). Formation processes of clathrate hydrates of carbon dioxide and methane. California Institute of Technology.

Bondarev, E., Rozhin, I., & Argunova, K. (2008). Prediction of Hydrate Plugs in Gas Wells in Permafrost. In *6th International Conference on Gas Hydrates*.

Chuvilin, E., Grebenkin, S., & Tkacheva, E. (2014). Change of gas permeability of gas-saturated sediments during hydrate formation and freezing.

Chuvilin, E. M., & Grebenkin, S. I. (2015). Gas permeability variation in gas-filled soils upon hydrate formation and freezing: an experiment study.

Ding, T., & Liu, Y. (2014). Simulations and analysis of hydrate formation during CO_2 injection into cold saline aquifers. *Energy Procedia*, *63*, 3030-3040.

Eaton, M., Mahajan, D., & Flood, R. (2007). A novel high-pressure apparatus to study hydrate–sediment interactions. *Journal of Petroleum Science and Engineering*, *56*(1), 101-107.

Engler, T. W., (2010). Fluid flow in porous media.

Freer, E. M., Selim, M. S., & Sloan, E. D. (2001). Methane hydrate film growth kinetics. *Fluid Phase Equilibria*, *185*(1), 65-75.

He, Y. (2012). Formation of methane and carbon dioxide hydrates in bulk and in porous media. TU Delft, Delft University of Technology.

Harrison, S. E. (2010). Natural Gas Hydrates. *Coursework Physics 240, Stanford University*.

Iglauer, S., Sarmadivaleh, M., Al-Yaseri, A., & Lebedev, M. (2014). Permeability evolution in sandstone due to injection of CO 2-saturated brine or supercritical CO 2 at reservoir conditions. *Energy Procedia*, *63*, 3051-3059.

Johnson, A., Patil, S., & Dandekar, A. (2011). Experimental investigation of gas-water relative permeability for gas-hydrate-bearing sediments from the Mount Elbert Gas Hydrate Stratigraphic Test Well, Alaska North Slope. *Marine and petroleum geology*, *28*(2), 419-426.

Jaiswal, N. J., Westervelt, J. V., Patil, S. L., Dandekar, A. Y., Nanchary, N. R., Tsunemori, P., & Hunter, R. B. (2004). Phase behavior and relative permeability of gas-water-hydrate system. In *AAPG Hedberg Conference on Gas Hydrates: Energy Resource Potential and Associated Geologic Hazards* (pp. 1-4).

Kantzas, A., Bryan., B, Taheri, S. (2017) Foundations of fluid flow in porous media.

Kneafsey, T. J. (2012). Examination of Hydrate Formation Methods: Trying to Create Representative Samples.

Kashchiev, D., & Firoozabadi, A. (2002). Driving force for crystallization of gas hydrates. *Journal of crystal growth*, *241*(1), 220-230.

Li, B., Li, X. S., & Li, G. (2014). Kinetic studies of methane hydrate formation in porous media based on experiments in a pilot-scale hydrate simulator and a new model. *Chemical Engineering Science*, *105*, 220-230.

Levine, J. (2011). Relative permeability experiments of carbon dioxide displacing brine and their implications for carbon sequestration. Columbia university.

Mork, M. (2002). Formation rate of natural gas hydrate-reactor experiments and models.

Mohebbi, V., & Mosayebi Behbahani, R. (2015). Measurement of Mass Transfer Coefficients of Natural Gas Mixture during Gas Hydrate Formation. *Iranian Journal of Oil & Gas Science and Technology*, *4*(1), 66-80.

Myre, D. (2011). Synthesis of carbon dioxide hydrates in slurry bubble column.

Mingjun, Y., Yongchen, S., Yu, L., Yongjun, Chen., & Qingping, L. I. (2010). Influence of pore size, salinity and gas composition upon the hydrate formation conditions. *Chinese Journal of Chemical Engineering*, *18*(2), 292-296.

Nam, S. C., Linga, P., Haligva, C., Ripmeester, J. A., & Englezos, P. (2008). Kinetics of hydrate formation and decomposition of methane in silica sand.

North, W. J., Blackwell, V. R., & Morgan, J. J. (1998). Studies of CO_2 hydrate formation and dissolution. *Environmental science & technology*, *32*(5), 676-681.

Nimblett, J., & Ruppel, C. (2003). Permeability evolution during the formation of gas hydrates in marine sediments. *Journal of Geophysical Research: Solid Earth*, *108*(B9).

Phirani, J., Pitchumani, R., & Mohanty, K. K. (2009). History matching of hydrate formation and dissociation experiments in porous media. In *SPE Reservoir Simulation Symposium*. Society of Petroleum Engineers.

Ruppel, C. (2011). Methane hydrates and the future of natural gas. *MITEI Natural gas Report, Supplementary Paper on Methane Hydrates*, *4*, 25.

Rajnauth, J. J., Barrufet, M., & Falcone, G. (2010). Potential industry applications using gas hydrate technology. In *Trinidad and Tobago Energy Resources Conference*. Society of Petroleum Engineers.

Schembre, J. M., Tang, G. Q., & Kovscek, A. R. (2006). Wettability alteration and oil recovery by water imbibition at elevated temperatures. *Journal of Petroleum Science and Engineering*, *52*(1), 131-148

Vysniauskas, A., Bishnoi, R. (1983). A kinetic-study of methane hydrates formation. Chem. Eng.Sci.38(7),1061−1072.

Vadla, E. R. (2015). An experimental study of methane hydrate growth and dissociation in porous media. Bergen University.

Vinci Technologies, Core flooding system – User guide Version 1.1. France.

Waite, W. F., & Spangenberg, E. (2013). Gas hydrate formation rates from dissolved-phase methane in porous laboratory specimens. *Geophysical Research Letters*, *40*(16), 4310-4315

Appendix A

A.1. Experimental data for water monophasic permeability

Table A.1.1. Experimental data of monophasic permeability for C1

Experiment 1		**Experiment 2**	
Q **(cm^3/min)**	**Delta *P*(psi)**	***Q*** **(cm^3/min)**	**Delta *P* (psi)**
0.1	39	0.1	42
0.15	54	0.15	57
0.22	84	0.22	87
0.34	128	0.34	131
0.50	193	0.50	197
0.75	288	0.75	293

Table A.1.2. Experimental data of monophasic permeability for C3

Experiment 1		**Experiment 2**	
Q **(cm^3/min)**	**Delta *P*(psi)**	***Q*** **(cm^3/min)**	**Delta *P* (psi)**
0.1	41	0.1	42
0.15	51	0.15	55
0.22	80	0.22	84
0.34	120	0.34	127
0.50	182	0.50	190
0.75	272	0.75	284

Table A.1.3. Experimental data of monophasic permeability for C4

Experiment 1		**Experiment 2**	
Q **(cm^3/min)**	**Delta *P*(psi)**	***Q*** **(cm^3/min)**	**Delta *P* (psi)**
0.1	15.4	0.1	23.9
0.15	25.3	0.15	32.4
0.22	42.7	0.22	45.7
0.33	67.8	0.33	65.6
0.50	102.0	0.50	95.1
0.75	154.3	#	#

Table A.1.4. Experimental data of monophasic permeability for C5

Experiment 1		**Experiment 2**	
Q **(cm^3/min)**	**Delta *P*(psi)**	***Q*** **(cm^3/min)**	**Delta *P* (psi)**
0.1	42	0.1	42
0.15	55	0.15	56
0.225	80	0.22	82
0.33	118	0.33	122
0.50	174	0.50	180
0.75	257	0.75	267

Table A.1.5. Experimental data of monophasic permeability for C6

Experiment 1		**Experiment 2**	
Q **(cm^3/min)**	**Delta *P*(psi)**	***Q*** **(cm^3/min)**	**Delta *P* (psi)**
0.1	69	0.1	62
0.15	109	0.15	102
0.22	159	0.22	154
0.33	237	0.33	232
0.50	351	0.50	345

A.2. Experimental data for the measurement of relative permeability at 20°C

Table A.2.1. First experimental data of relative permeability measurements at 20ºC for C1

P_1 (psi)	P_2 (psi)	Q (cm^3/min)	m (g/min)
246	181	2.334	0.05835
314	182	5.55	0.13875
380	183	9.318	0.23295
468	181	14.62	0.3654

Table A.2.2. Second experimental data of relative permeability measurements at 20ºC for C1

P_1 (psi)	P_2 (psi)	Q (cm^3/min)	m (g/min)
301	185	5.358	0.13271
368	183	6.264	0.15516
442	183	11.496	0.28476
549	183	17.274	0.42787

Table A.2.3. Experimental data of relative permeability measurements at 20ºC for C3

P_1 (psi)	P_2 (psi)	Q (cm^3/min)	m (g/min)
257	197	1.33	0.0359
343	197	5.22	0.1409
391	196	6.99	0.1889
452	196	9.606	0.2593
500	197	14.4	0.3888

Table A.2.4. First experimental data of relative permeability measurements at 20ºC for C4

P_1 (psi)	P_2 (psi)	Q (cm^3/min)	m (g/min)
257	184	3.331	0.08300
327	185	9.27	0.2310
379	184	11.49	0.2863
431	185	12.97	0.3232
468	182	14.34	0.3573
518	182	23.2	0.5781

Table A.2.5. Second experimental data of relative permeability measurements at 20ºC for C4

P_1 (psi)	P_2 (psi)	Q (cm^3/min)	m (g/min)
249	196	2.616	0.0693
308	194	5.09	0.1348
352	193	8.268	0.2191
416	195	13.53	0.3585
485	196	22.926	0.6075

Table A.2.6. Experimental data of relative permeability measurements at 20ºC for C5

P_1 (psi)	P_2 (psi)	Q (cm^3/min)	m (g/min)
284	178	1.8	0.0432
337	178	3.82	0.09168
416	180	7.266	0.1744
481	178	9.35	0.2244

Table A.2.7. Experimental data of relative permeability measurements at 20ºC for C6

P_1 (psi)	P_2 (psi)	Q (cm^3/min)	m (g/min)
354	181	1.932	0.0477
419	182	4.69	0.1158
487	182	7.374	0.1821
563	184	11.376	0.2809

A.3. Experimental data for the measurement of the relative permeability under hydrate forming conditions

A.3.1. Experimental data at 4ºC

Table A.3.1.1. First experimental data of relative permeability measurements at 4ºC for C4

P_1 (psi)	P_2 (psi)	Q (cm^3/min)	m (g/min)
310	214	7.428	0.23836
354	215	9.74	0.31255
429	217	17.28	0.55451
564	215	35.6	1.1424
640	215	3.4	0.1091
681	213	4.59	0.14729

Table A.3.1.2. Second experimental data of relative permeability measurements at 4ºC for C4

P_1 (psi)	P_2 (psi)	Q (cm^3/min)	m (g/min)
282	218	6.696	0.218222
400	220	17.418	0.56765
452	219	14.6	0.47581
547	218	0.45	0.01466
597	216	0.984	0.032068
647	214	0.024	0.000782

Table A.3.1.3. Third experimental data of relative permeability measurements at 4ºC for C4

P_1 (psi)	P_2 (psi)	Q (cm^3/min)	m (g/min)
300	226	7.2	0.24408
358	227	12.64	0.42976
406	227	16.9	0.5746
458	225	20.88	0.703656
536	226	7.71	0.261369
600	215	0.054	0.00173

Table A.3.1.4. Experimental data of relative permeability measurements at 4ºC for C3

P_1 (psi)	P_2 (psi)	Q (cm^3/min)	m (g/min)
237	195	2.52	0.07250
271	195	2.832	0.08148
322	201	4.11	0.12231
371	202	4.542	0.13581
413	201	4.74	0.14106
464	203	4.6	0.13846
520	201	1.212	0.03607

Table A.3.1.5. Experimental data of relative permeability measurements at 4ºC for C1

P_1 (psi)	P_2 (psi)	Q (cm^3/min)	m (g/min)
245	207	1.494	0.04586
291	207	3.84	0.1178
340	208	2.922	0.09028
380	207	3.09	0.0948
431	207	2.472	0.07589
494	206	1.584	0.04847
519	206	0	0

Table A.3.1.6. Experimental data of relative permeability measurements at 4ºC for C5

P_1 (psi)	P_2 (psi)	Q (cm^3/min)	m (g/min)
286	209	2.178	0.067518
325	209	4.56	0.14136
360	209	6.468	0.200508
423	208	2.172	0.067332
486	208	2.61	0.08091
563	208	0.132	0.004092

A.3.2. Experimental data at 3ºC

Table A.3.2.1. Experimental data of relative permeability measurements at 3ºC for C4

P_1 (psi)	P_2 (psi)	Q (cm^3/min)	m (g/min)
293	219	3.948	0.13068
339	220	3.054	0.10109
386	220	3.384	0.11201
441	220	2.406	0.07963
501	216	0.042	0.00136

Table A.3.2.2. Experimental data of relative permeability measurements at 3ºC for C1

P_1 (psi)	P_2 (psi)	Q (cm^3/min)	m (g/min)
238	201	0.66	0.019734
284	201	1.542	0.0461058
323	202	1.536	0.04608
362	202	2.154	0.06462
405	201	1.938	0.0579462
463	201	1.59	0.047541
498	199	0.75	0.022125

Table A.3.2.3. Experimental data of relative permeability measurements at 3ºC for C3

P_1 (psi)	P_2 (psi)	Q (cc/min)	m (g/min)
274	198	3.252	0.09560
317	198	4.782	0.14059
358	199	6.072	0.1791
395	199	6.252	0.1844
457	198	2.574	0.07567
516	189	0.522	0.01456

A.4. Experimental data of water monophasic permeability after flooding of CO_2 at 20ºC

Table A.4.1. Experimental data of monophasic permeability measurements at 20ºC for C1 after flooding CO_2

Q **(cm^3/min)**	**Delta *P* (psi)**
0.1	38.6
0.15	48.8
0.22	69.2
0.33	99.5
0.50	146.2
0.75	212.5

Table A.4.2. Experimental data of monophasic permeability measurements at 20ºC for C3 after flooding CO_2

Q **(cm^3/min)**	**Delta *P* (psi)**
0.1	39.1
0.15	50.8
0.22	72.1
0.33	104.1
0.50	153.0

Table A.4.3. Experimental data of monophasic permeability measurements at 20ºC for C4 after flooding CO_2.

Q **(cm^3/min)**	**Delta *P* (psi)**
0.1	25.7
0.15	34.1
0.225	46.1
0.33	64.2
0.50	90.9
0.75	130.3

Table A.4.4. Experimental data of monophasic permeability measurements at 20ºC for C4 after flooding CO_2.

Q **(cm^3/min)**	**Delta *P* (psi)**
0.1	47.5
0.15	60.3
0.22	86.9
0.33	126.1
0.50	183.9
0.75	268.9

Table A.4.5. Experimental data of monophasic permeability measurements at 20ºC for C5 after flooding CO_2.

Q **(cm^3/min)**	**Delta *P* (psi)**
0.1	78.5
0.15	108.4
0.225	163.5
0.33	246.7
0.50	371.5

Appendix B

B.1. Wallace Quarries – Test Data

Wallace Quarries - Test Data

Testing Data For Wallace Sandstone

Results of ASTM testing carried out by National Research Council, Halifax, Nova Scotia. March 1967.

Absorption	Percent absorption after 24 hrs. was 4.0%
Saturation Coefficient	Saturation Coefficient was 0.644
Unit Weight	Unites varies from 141.0 lbs cu/ft to 145 lbs. cu/ft for 12 specimens tested.
Porosity	The apparent porosity was 14.3%
Compressive Strength	On four specimens of sandstone compressive strength ranged from 11,154 PSI to 14,759 PSI
Freeze - Thaw Test	Fifty freeze - thaw test were completed on four samples with no failures. The average weighted lossat the end of cycling was 0.06%

Results of mineral analysis carried out by Dalhousie University (Mineral Engineering Center) Halifax, Nova Scotia. February 19th, 2001.

SiO2	Silicon Dioxide	"Silica"	82.00 %
Al2O3	Aluminium Oxide	"Alumina"	8.12 %
Fe2O3	Ferric Oxide	"Hematile"	3.19 %
Na2O	Sodium Oxide		1.67 %
K2O	Potassium Oxide		1.13 %
MgO	Magnesium Oxide		0.72 %
CaO	Calcium Oxide		0.81 %
TiO	Titanium Oxide	"Titania"	0.29 %
MnO	Manganese Oxide	"Magnesia"	0.10 %
L.O.I.	Loss on Ignition		2.59 %

If additional information is required, please contact Wallace Quarries Ltd.

Email: flynn@wallacequarries.com
Phone: 1-902-257-2014

Mailing Address:
Wallace Quarries Ltd.
P.O. Box 203
Wallace, Nova Scotia, Canada
B0K 1Y0

B.2. The variation of viscosity and compressibility factor with pressure at different temperature

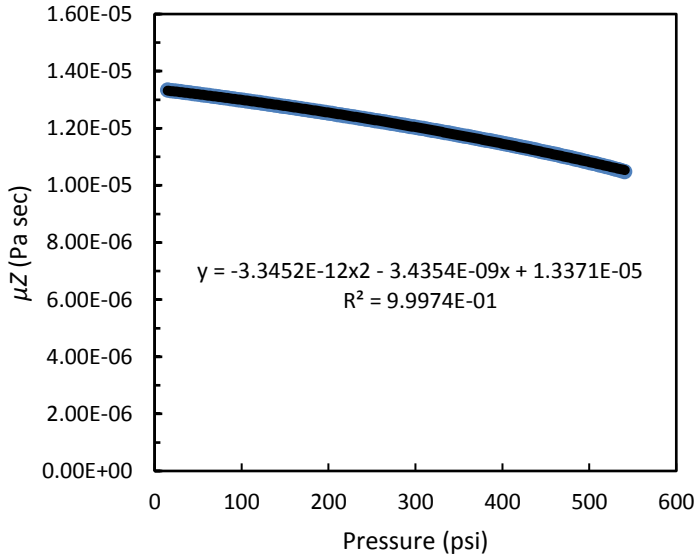

Fig. B.2.1: Variation of viscosity and compressibility factor with pressure at 3ºC.

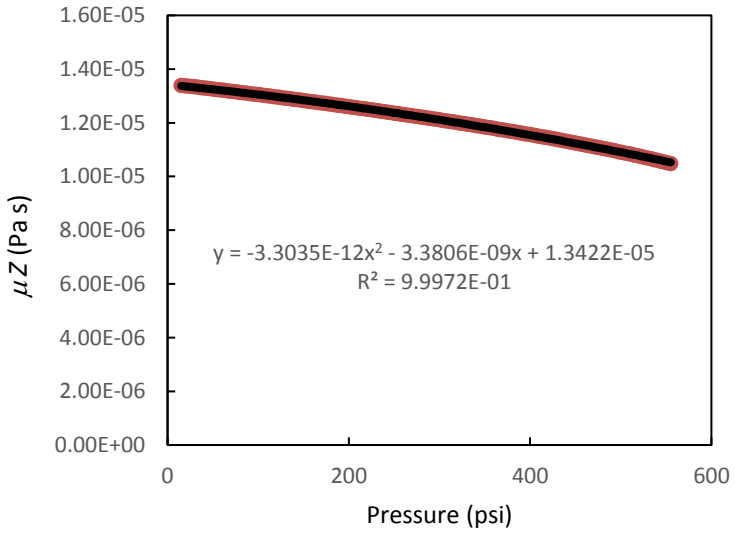

Fig. B.2.2: Variation of viscosity and compressibility factor with pressure at4ºC.

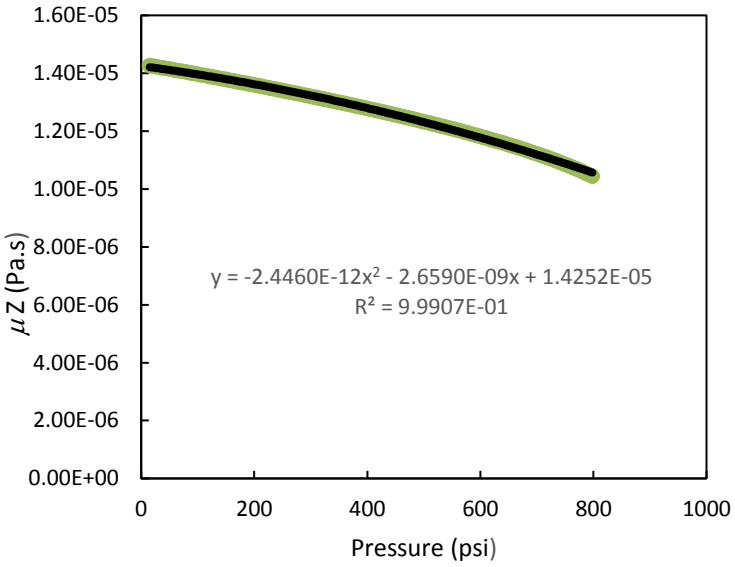

Fig. B.2.3: Variation of viscosity and compressibility factor with pressure at 20ºC.